The complex 4D multi-segmented rupture of the 2014 M_w 6.2 Northern Nagano Earthquake revealed by high-precision aftershock locations

Titouan Muzellec[(1)], Grazia De Landro[(1)], Giovanni Camanni[(2)], Guido Maria Adinolfi[(3)] and Aldo Zollo[(1)]

(1) Università degli Studi di Napoli "Federico II", Dipartimento di Fisica E. Pancini, RISSC-Lab, Naples, Italy

(2) Università degli Studi di Napoli "Federico II", DiSTAR, Naples, Italy

(3) Università degli Studi di Torino, Dipartimento di Scienze della Terra, Turin, Italy

Correspondence to: Titouan Muzellec (titouan.muzellec@unina.it)

Key points:

- High accurate spatio-temporal evolution of Northern Nagano sequence by double-difference locations in three-dimensional velocity models.
- Reconstruction of 4D evolution of the complex fault segmentation.
- The initial structure of the segmented fault system has key controls on seismicity evolution and length of the earthquake rupture.

Abstract

Neglecting fault segmentation in hazard assessments leads to underestimated potential hazard. Moreover, integrating the temporal evolution of fault segments activations in hazard assessment improve scenario's reliability. In this view, enhanced seismic catalogs have potential in revealing previously neglected fault complexities. Past efforts were restricted to the 2D view analysis without involving the segment temporal activation. Our work provides a comprehensive approach, reconstructing 3D fault fine-scale geometry and segments activation evolution.

We analyzed the 2014 Northern Nagano (Japan) (M_w 6.2) earthquake sequence using high-resolution seismic catalogs. We automatically detected and located about 2500 events between October and December 2014. We refined the automatic picks, based on cross-correlation and hierarchical clustering, and we relocated the hypocenters with the double-difference in 3D velocity models optimized for the area. Moreover, we calculated the composite focal mechanisms of the main clusters, crucial to constrain the 3D geometry of the fault segments, and rupture directivity that we interpreted jointly with the seismicity and the fault slip. We found that the multi-segmented fault system, is comprised of, at least, 9 distinct segments, that ruptured during 3 successive phases. Different segments exhibit a different rupture mechanism based on their spatial and temporal occurrence, influencing seismicity evolution and rupture length. The presented analysis can be used to improve the reliability of probabilistic hazard assessment in the high seismic potential area of the Itoigawa-Shizuoka fault system. The possibility of fault segment interaction and mutual triggering processes should be considered when drawing reliable seismic hazard scenarios.

Plan Language Summary

The development of realistic rupture scenarios of moderate-to-large earthquakes highlights the need of integrating their 3D geometrical complexities and the temporal evolution of fault segments activation. In this view, we analyzed the M_w 6.2 earthquake sequence that occurred in the Northern region of

Nagano (Japan) to reconstruct the 3D geometry of the fault surface and the evolution of segments activation. Based on the continuous records of 37 seismic stations from 1st October 2014 to 31 December 2014, a refinement picking procedure based on waveforms similarity, a three-dimensional velocity model, and a double-difference location method were used to locate around 2500 events. The high-quality earthquake location catalog and composite focal mechanisms constrain the three-dimensional geometry of the segmented fault system with at least 9 distinct segments activated in succession during 3 phases. The early aftershocks exhibit a broad NNE-SSW structure located at shallow depth, involving first the shallow northern and southern portions of the segmented surface, then the deeper northern portion of it, and finally the deeper part of the southern portion. The complexity of the fault system suggests improving the way in which we characterize the fault systems by considering how the fault segmentation controls the earthquake rupture.

1. Introduction

In the last decades, several significant earthquakes (e.g., 2008 M_w 8.0 Wenchuan, China: Lin et al., 2009; 2016 M_w 7.8 Kaikōura, New Zealand: Ulrich et al., 2019; 2023 M_w 7.8 and M_w7.6 Kahramanmaraş earthquake doublet, Turkey: Karabacak et al., 2023; Özkan et al., 2023; Petersen et al., 2023; Reitman et al., 2023; Toker et al., 2023) have highlighted a common behavior: large earthquakes often involve multiple fault segments rather than individual, unsegmented fault surfaces. This has a strong impact on hazard assessment, especially related to the occurrence of large magnitude aftershocks. Hazard is highest for the segmented fault model, in which seismic moment is accommodated by frequent moderate (moment magnitude M_w 6.2-6.8) earthquakes. The unsegmented model yields the lowest average seismic hazard because part of the seismic moment is accommodated by large (M_w 6.9–7.9) but infrequent ruptures (Iacoletti et al., 2021). Hence, it is crucial to characterize the segmentation of capable faults. Fault segment interaction and their mutual static triggering activation is a prominent mechanical process during the aftershock occurrence, whose impact could be strongly underestimated if not considered in the hazard evaluation. Beside fault segmentation, other significant aspects for a reliable estimation of hazard are the inclusion of time-dependent occurrence

of segments activation, and the account for their mutual interaction (see Iacoletti et al. 2021 and the references therein).

With the objective of characterizing the complexity of fault structures across various scales, numerous efforts have been undertaken using different datasets, including field and seismic reflection data (see, for example, Peacock and Sanderson, 1991; Huggins et al., 1995; Childs et al., 1996; Nicol et al., 2002; Walsh et al., 2003; Wesnousky, 2006; Camanni et al., 2019, 2023a,b; Delogkos et al., 2020; Roche et al., 2021), as well as seismological data (Wesnousky, 1988; Manighetti et al., 2007, 2009; Hamling et al. 2017; Cesca et al. 2017; Improta et al., 2019; Ross et. al 2019; Michele et al. 2020; Waldhauser et al. 2021; Roche et al., 2022). The availability of enhanced seismic catalogs containing precisely located events has allowed for revealing of previously neglected fault structural complexities (Chiaraluce et al., 2003; Valoroso et al., 2014; Cesca et al., 2017; Tondi et al., 2020).

However, most of the studies based on seismological data typically characterize fault segmentation in two dimensions (2D), either through mapping (e.g., Cesca et al. 2017) or in cross-section (e.g., Valoroso et al. 2014; Waldhauser et al. 2021), without accounting for lateral variation of fault geometry. Moreover, these studies do not incorporate the temporal activation or potential interaction of fault segments into the reconstruction of their characteristics.

Here we provide a comprehensive and integrated approach to reconstruct the 3D fine-scale geometry of fault system and the evolution of segments activation (i.e., fourth dimension) starting from an enhanced catalog of foreshock-mainshock-aftershock sequence over a time interval extending beyond the early aftershocks (i.e., several months). We selected the November 2014 Northern Nagano earthquake (M_w 6.2), Japan, as it involved a prolonged and complex foreshock and aftershock sequence associated with more than 2000 events activating a complex segmented fault system (Panayotopoulos et al., 2016; Imanishi and Uchide, 2017).

In this work, we explored the mechanism of the mainshock-aftershock sequence by using high precision earthquake locations, to (i) propose an improved three-dimensional (3D) model of the segmented fault system, and to (ii) characterize the 4D evolution of the rupture on the segmented fault

system during the 1-month aftershock sequence. First, we built an enhanced seismic catalog by applying a procedure for the event detection and location to the continuous data from 1st October 2014 to 31 December 2014. Then, we refined the automatic absolute picks with a new technique based on waveform similarity and hierarchical clustering. The high-resolution earthquake locations were obtained by double difference (DD) technique and 3D velocity models optimized for the area. The seismicity pattern, combined with newly calculated composite focal mechanisms of significant clusters, were in turn used to derive the 3D geometry of the different fault segments activated during the mainshock rupture and in the following weeks. This data provided a new image of the 4D occurrence and the clustering of the events that characterized the rupture evolution of the complex fault system activated into 3 main phases during the 2014 Nagano earthquake sequence.

The reconstructed 4D fault model revealed the fine-scale complexity of the segmented rupture process during the aftershock sequence and can be used as source model in the mainshock-aftershock hazard evaluation framework for a more reliable assessment in the Itoigawa-Shizuoka, high potential fault system where another significant earthquake of M_w 7.5 has recently occurred on January,1, 2024. Besides, the proposed approach can be extended to other high-risk areas to properly evaluate the main pieces of information for a comprehensive characterization of fault complexity and a reliable assessment of seismic hazard.

2. The setting of the Mw 6.2 Northern Nagano Earthquake Sequence

The tectonic setting of the study area is dominated by the Itoigawa-Shizuoka tectonic line (ISTL), which crosses the Honshu Island and extends for ~ 150 km from Itoigawa City on the Sea of Japan to Shizuoka City on the Pacific Ocean (see Fig. 1). The ISTL roughly strikes NNE–SSW to NNW–SSE and is one of the most active faults in Japan, since it forms one arm of the triple junction between the Eurasian, North American, and Philippine Sea plates. In the north, within the study area, the ISTL is made up of at least two major, nearly N-S striking, sub-parallel branches: the Kamishiro fault (KF, Fig. 1) in the West, and the Otari–Nakayama fault (OTNF, Fig. 1) in the East. Both faults developed

as the bounding, east-dipping extensional faults of the Northern Fossa Magna (NFM) rift basin (Sato, 1994), which formed during the final extensional stages of the opening of the Japan's Sea (25 – 15 Ma) (Otofuji et al., 1985; Yamaji, 1990), and juxtapose sedimentary rocks of the basin infill in the East against older basement rocks of the "inner zone" (INZ) in the West. The NFM basin comprises 5-6 km thick Miocene marine sediments (Kato, 1992; Takano, 2002; Panayotopoulos et al., 2013); the INZ is made up largely of pre-Neogene basements rocks comprising Paleozoic-Mesozoic accretionary complex and granitic rocks (Fig. 1) (Kano et al., 1990; Taira, 2001).

Since the Pliocene (ca. 3 Ma) an inversion of the stress field in central Japan resulted in the ongoing inversion of the NFM rift basin through the reactivation of its bounding fault system with an overall reverse kinematics (Williams et al., 1989; Sato, 1994; Sato, 1996). The KF has been shown to be currently an active thrust fault (e.g., Sato et al., 2004; Takeda et al., 2004). On the other hand, the OTNF, shows no geomorphological evidence of late Quaternary activity (Matsuta et al., 2004).

The M_w 6.2 mainshock of the here studied seismic sequence occurred at the Northern Nagano prefecture on the 22 November 2014 at 10:08 pm JST (01:08 pm UTC). The epicenter of the mainshock is located nearby the KF and OTNF faults (red star in Fig. 1), and the estimated focal mechanism from the centroid moment tensor (CMT) solution, given by the Japan Meteorological Agency (JMA) and by the National Research Institute for Earth Science and Disaster Resilience (NIED), shows a reverse faulting with a left-lateral component (JMA, 2014; NIED, 2014). A foreshock activity has been detected near the mainshock location during the 4 days before its occurrence. As mentioned by Imanishi and Uchide (2017), the 4D evolution of the foreshock activity is characterized by seismicity migration from the shallow crust to the mainshock location. Imanishi and Uchide (2017) interpreted that the mainshock was triggered by the stress loading caused by the foreshock activity driven by aseismic slow slip.

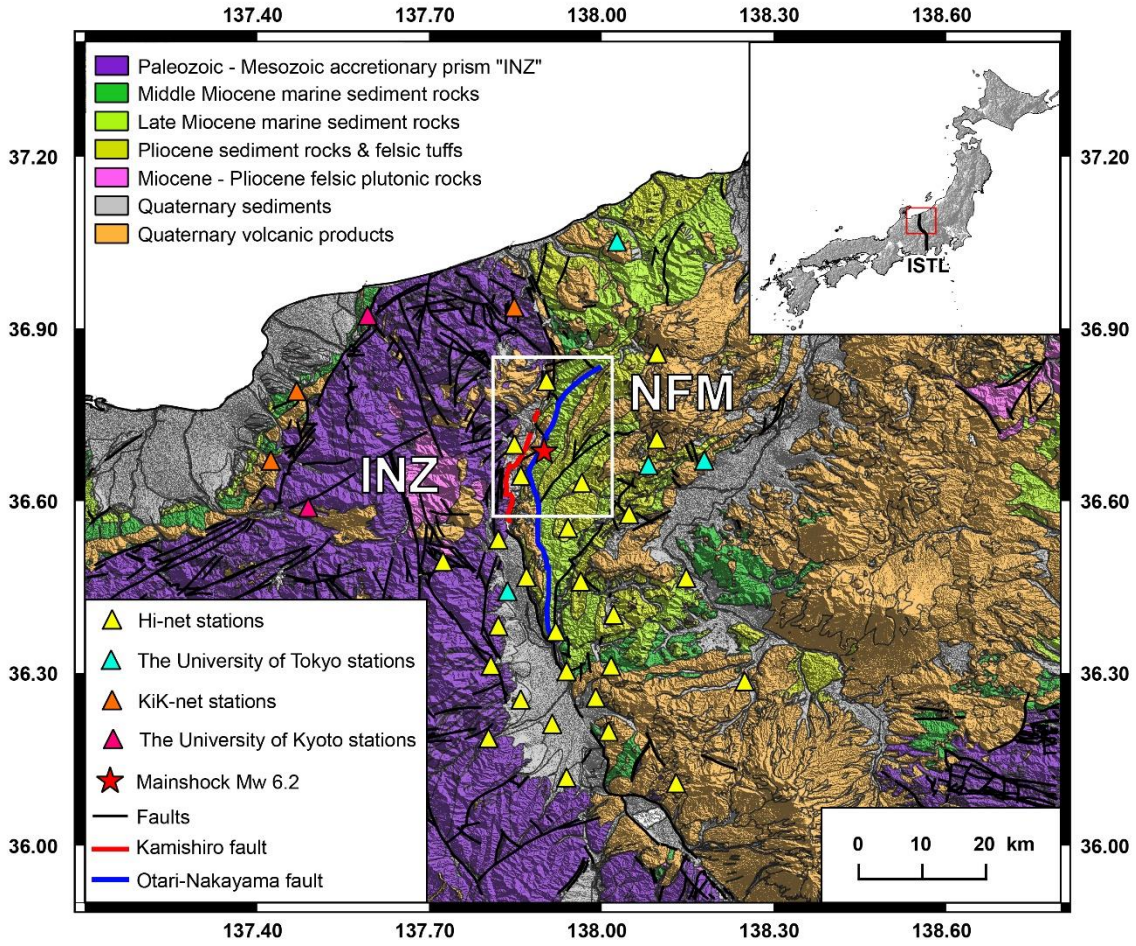

148

149

150 **Figure 1**. Geological map of the area surrounding the 2014 Nagano earthquake sequence,
151 modified from Panayotopoulos et al. (2016). Red star indicates the M_w 6.2 mainshock
152 location. Triangles indicate the location of the seismic stations used in this study. White
153 rectangle indicates the studied area. Northern Fossa Magna (NFM), Inner Zone (INZ),
154 Itoigawa-Shizuoka tectonic line (ISTL).

155

156 Most of the surface ruptures related to the mainshock followed the mapped surface trace of the KF
157 (Okada et al., 2015). Several studies used interferometric synthetic-aperture radar (InSAR)
158 (Panayotopoulos et al., 2016; Ando et al., 2017; Kobayashi et al., 2018) to identify the surface

displacement observed after the mainshock and interpreted the slip distribution as associated with a non-planar east-dipping fault formed by KF and OTNF faults. Similarly, by using the relocated hypocenter of a part of the aftershock activity, Panayotopoulos et al. (2016) determined the source fault model as composite, with a shallow part corresponding to the KF with a dip of 30°-45°, and a deeper portion corresponding to the deep part of the OTNF with a dip of 50°-60°, resulting in an overall bending, steepening downward fault planar surface. Ando et al. (2017) confirmed this bending planar fault structure and added some branch faults with different bends for the different clusters around the main fault to fit reasonably the surface deformation data. The relocated aftershocks by Panayotopoulos et al. (2016) show a clear difference in seismicity distribution between the northern and the southern part of the earthquake sequence area. The gap of aftershocks on the surface rupture is consistent with several studies showing aftershocks concentration at the margin of asperity (Okada et al., 2015) where the coseismic slip is low (Panayotopoulos et al., 2016). Indeed, Ando et al. (2017) show a high coseismic slip patch in the south of the earthquake sequence at shallow depth. This correlation of high slip patch on the fault and low concentration of aftershocks, which has been observed for other major earthquakes in Japan (Hirata et al., 1996; Asano et al., 2011), is related to the total stress release on this patch of the fault.

3. Data and Methods

3.1. Refinement picking

In this study we used continuous seismic data recorded from 1st October to 31 December 2014 by 27 short period three component velocity seismometers of the permanent network Hi-net (NIED, 2019) operated by the NIED and JMA, 4 seismometers operated by the University of Tokyo, 3 strong-motion seismograms of the permanent network KiK-net and 2 seismometers operated by the University of Kyoto (triangles in Fig. 1). First, we applied an optimized strategy to chain existing methods for the automatic detection (Adinolfi et al., 2020), picking, and location of events, we used LASSIE (Heimann et al., 2017) PHASE (Ross & Ben-Zion 2014) and MParloc (Zollo et al., 2021),

respectively, following the same approach of Adinolfi et al (2020, 2022, 2023). This allowed us to construct a homogeneous initial catalog of 2477 events through the whole period of three months with a magnitude range between -0.6 and 6.2 (see Fig S1 in SM).

It is well known that automatic pick tools can introduce systematic shifts to the output pick distribution (Lois et al., 2013; Baillard et al., 2014). This affects, not only the quality of the initial catalog location, but also the accuracy of differential travel-times measurements, that depend on the event origin time. To obtain high quality DD locations, we applied the refinement picking procedure based on waveform similarity and hierarchical clustering, on the first set of automatic absolute picks. We measured through cross-correlation (CC) the similarity between waveforms of the filtered seismic records to build families of similar events with hierarchical clustering. Within each family, we constructed a reference trace (RT), by the weighted stack of all the waveforms, on which automatically measured a refined pick used as reference to correct the picks of other events in the family (for further details see section A1 in SM). This procedure is constructed to mitigate both the inconsistency among picks on similar waveforms and the systematic shift introduced by automatic picking tools (Fig. 2a). By looking at the increase of signal to noise ratio (SNR) calculated around refined picks, respect the one of initial picks, (Fig. S2 in SM) we can assess that we improved our pick quality.

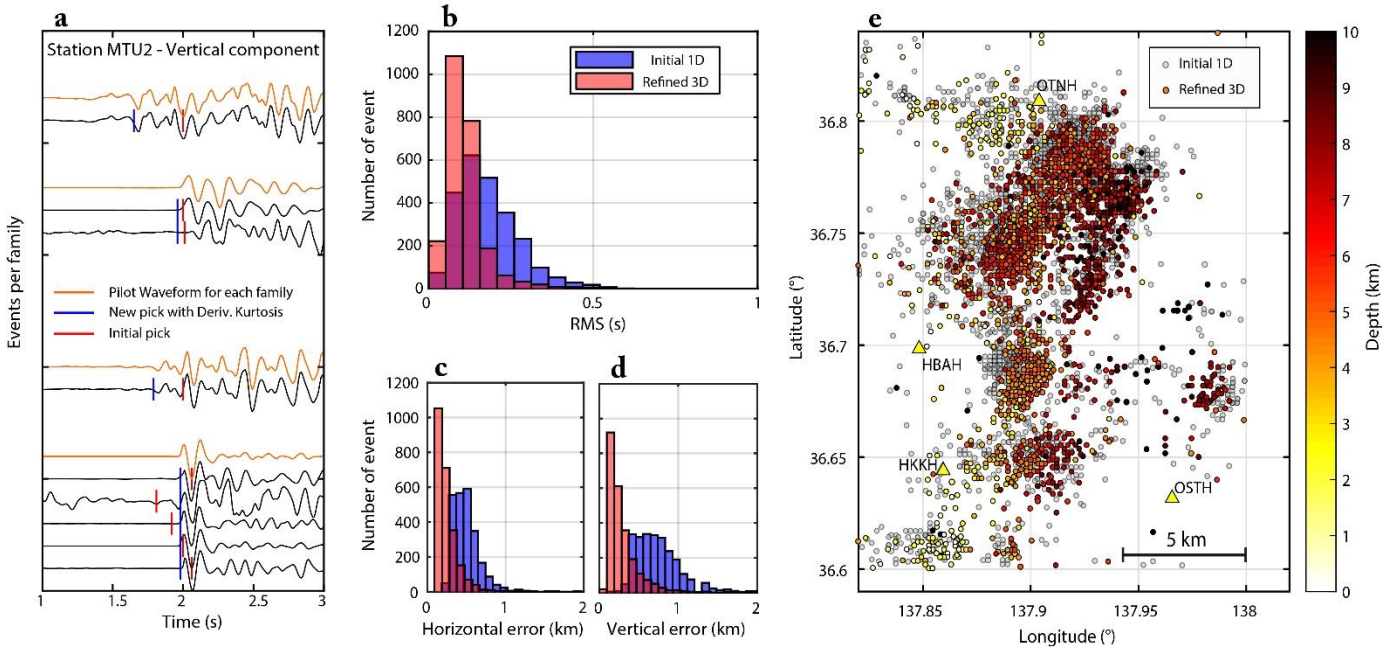

Figure 2. (a) Seismic traces recorded on the vertical component at one station classified in family belonging. The orange trace is the RT of each family. Vertical blue line indicates the position of the refined P arrival time. Vertical red line indicates the position of the initial P arrival time. (b) Histogram of the root mean square (RMS) from the absolute locations. (c) Same as be for the horizontal error. (d) Same as (b) for the vertical error. (e) Relocate absolute seismicity of the 2014 Nagano earthquake sequence by using the 1D/3D velocity models and the initial/refined arrival time picks.

3.2. Earthquake locations

To improve the hypocenter location, we followed a three steps process:

1) First, we estimated the absolute hypocenter locations with NonLinLoc software (Lomax et al., 2009) in the 1D velocity model used for the JMA Unified Earthquake Catalog (JMA, 2014), by inverting initial automatic picks and refined ones. Then we relocated the seismicity in DD by using HypoDD (Waldhauser and Ellsworth, 2000) and considering the CC and catalog differential times. The CC differential travel times was calculated between events within families built during the refinement picking procedure.

2) To further improve our location quality, we constructed 3D P- and S- waves velocity models by inverting arrival times through a linearized tomographic approach. We used the code TOMOTV (Latorre et al. 2004), well consolidated since applied in different environments and at different scales (De Landro et al. 2020, 2022; Amoroso et al. 2022). In our strategy, we inverted the refined picks by starting from the 1D velocity model from JMA (JMA, 2014) (see section A2 in SM). By looking the map view of the velocity models (Figure S3.1-2), there is a strong east-west variation of velocity in the first kilometers depth. The geological structure related to the low velocity zone should end between 4 and 7 km depth. By comparing the position of the velocity anomalies and the geological features at the surface, the low velocity anomaly on the east side of the fault system is related to the NFM basin while the high velocity anomaly of the west side of the fault corresponds to the INZ (basement structure).

3) In the next step, we located the hypocenters in 3D velocity models (Fig. S3.1-2 in SM) with NonLinLoc (Lomax et al., 2009), we computed the CC differential times by considering refined location and, then we relocated the seismicity with HypoDD by inverting CC and catalog differential times (see section A2 in SM).

The high consistency of the refined phase picks allows to increase the accuracy of absolute location by reducing the root-mean-square (RMS) from 0.19 s to 0.11 s (Fig.2b) and the mean location error from 0.6 km to 0.2 km (Fig.2c-d). This result is a further confirmation of the improvement of pick quality consequent to the application of the refinement procedure. It is interesting to note that with 3D absolute locations we observed a clustering of events and a shift of the seismicity toward the east comparable with the features previously observed with the use of DD location (Fig.2d; Panayotopoulos et al., 2016). To minimize the effect of the global harmonization of the 3D model at large parametrization, we focused the analysis on the hypocenter location determined by relative travel times based on the location with the 3D velocity model. With the last location step, we reduced the location errors for DD to an average of about 100 meters (see section A2 and Fig. S4 in SM).

3.3 Rupture directivity

242 We used the 23 strong motion records of the M_w 6.2 Northern Nagano earthquake acquired by the
243 near-source strong-motion seismograph from Kiban Kyoshin Network (KiK-net) operated by the
244 NIED (NIED, 2019) to infer the mainshock rupture geometry and propagation mode (see section A3
245 and Fig. S5 in SM). With this aim the method proposed by Convertito et al. (2012) has been applied to
246 invert the recorded Peak Ground Velocity (PGV) data to determine the fault length (in terms of its
247 surface projection), the dominant rupture mode (uni- or bi-lateral), direction and velocity.

248 For this analysis we assumed the moment magnitude M_w 6.2 and used the PGV data measured from
249 the 0.1-3 Hz band-pass filtered accelerograms recorded by the 23 near-source stations of the strong
250 motion network. PGV data are preliminary corrected for the distance attenuation effect, by multiplying
251 each data by the hypocentral distance, then the optimal rupture parameters (rupture length L,
252 predominant rupture length L', Mach number α and the rupture direction) are determined through a
253 Bayesian probabilistic inversion method based on a grid search model parameter exploration
254 (Convertito et al., 2012). The final PGV residual distribution confirms the consistency of the retrieved
255 model with observations indicating a well peaked residual distribution around zero with a net
256 improvement relative to the directivity of un-modeled data (see Fig. S5 in SM).

257 ### 3.4 Composite focal mechanisms

258 To determine in detail the fault geometry and confirm the fault delineation highlighted by the
259 seismicity, we computed the composite focal mechanism with the program FPFIT (Reasenberg, 1985)
260 for several clusters by reducing the uncertainty of the polarity measurements that can be done for
261 single event. By the contribution of the polarity measurements of each event among the same cluster,
262 FPFIT calculates the best fault-plane solution with a weighted sum of the first P-wave polarity
263 discrepancies (Aki and Richards, 2002). For this analysis, we evaluate the composite focal mechanism
264 by selecting co-located events belonging to 9 significant clusters with a total of 1053 events. We
265 selected the clusters based on the event's 4D proximity, by focusing especially on the small-scale
266 features of the seismicity pattern not detected in previous works (Panayotopoulos et al., 2016). We
267 manually measured the polarities at least for the 8 closest seismic stations from the earthquake

sequence location. The results can be found in table S1 of SM. The obtained focal mechanisms are well constrained, and the average error strike, dip, and rake is about 7°, 11°, and 12° respectively (see Fig. S6-14 in SM).

4. 4D seismicity evolution

Hypocenters of the relocated mainshock and aftershocks are shown in Fig. 3, 4, and 5. In Fig. 3 we show the map view, the sections, and distribution along the strike of the fault structure of the aftershocks over the entire period. The mainshock of the Nagano sequence occurred on 22 November 2014 at 01:08:17.56 pm (UTC) in correspondence of the northern tip of the southern segment involved in the rupture (red star in Fig. 3,4a-b) at 3.3 km of depth. The relocation procedure allowed us to reach an unprecedented precision in the location of the mainshock, with location errors of the order of a few hundred meters (see section A2 in SM), especially in depth by considering the use of an optimized 3D velocity model. By looking at the aftershock distribution (Fig. 3), we can note the distribution is following a striking structure N20° oriented and the higher number of aftershocks in the northern part of the earthquake sequence compared to the southern part. By looking the sections, most of the aftershocks are distributed in several clusters that we can clearly identify spatially (see sections on Fig. 3). In the southern part, the seismicity follows a single fault plane with a main cluster around the mainshock location. In the northern part, the clusters identified are globally deeper than the clusters identified in the southern part. Also, we can note some clusters are activated by a major shock (with a $M_{JMA} \geq 4$, green stars on Fig. 3). The temporal distribution of seismicity along the strike (Fig. 3) shows the temporal feature only for the shallower clusters/segments activated by a major shock. The aftershocks distribution among several clusters/segments, activated at different time and probably affected by several triggering mechanisms, show the complexity of the fault related to the main rupture.

To constrain the geometry of the faults involved in the Nagano sequence, previous analyses have been based on the calculation of focal mechanisms for major shocks in different sectors of the system

294 (JMA, 2014; NIED, 2014; Panayotopoulos et al., 2016). Here, we take advantage of the density, we
295 consider a longer time period, and the quality of the obtained seismic catalog, to calculate composite
296 focal mechanisms for events belonging to 9 significant clusters involving up to 1053 events.

297 To describe the pattern of the seismicity and catch the activation of the fault segments involved, we
298 selected 4 different time intervals (see table 1) that we used in Figure 4 and 5. In Fig. 4 we show the
299 sequence evolution (Fig. 4a-e), together with the results of rupture directivity analysis (Fig. 4a) and
300 composite focal mechanism for significant clusters (Fig. 4f). In Fig. 5 we show 4 vertical sections
301 through the same data and at the same time intervals.

302 By analyzing the seismicity within the different time intervals (Fig. 4 and 5), we can define 3 main
303 phases with the first phase about the seismicity related to the main rupture at coseismic time-scale
304 (mainshock rupture and 3h aftershocks), the second phase, within the week after the mainshock
305 occurrence, characterized by the deep segments activation in the northern part, and the third phase
306 within the month after the mainshock occurrence, characterized by the activation of deep part of the
307 fault in the southern part.

308

309 **Table 1**. Description of selected time periods. In the first column the time is referred to the

Phase	Time Interval	Correspondent date (UTC)
1	From MOT to 1 h after	From 14/11/22 01:08:17.56 pm to 14/11/22 02:08:17.56 pm
1	From 1 h to 3 h after MOT	From 14/11/22 02:08:17.56 pm to 14/11/22 04:08:17.56 pm
2	From 12h to 24h after MOT	From 14/11/23 01:08:17.56 am to 14/11/23 01:08:17.56 pm
2	From 24h to one week after MOT	From 14/11/23 01:08:17.56 pm to 14/11/30 11:59:59 pm
3	From one week to one month after MOT	From 14/12/01 00:00:00 am to 14/12/31 11:59:59 pm

310 mainshock origin time (MOT), 22 November 2014 at 01:08:17.56 pm (UTC).

311

312 4.1. Phase 1 / Mainshock rupture

313 The early aftershocks, first hours after the mainshock origin time (MOT), which better highlight the
314 geometry of the mainshock rupture, are distributed along a broad NNE-SSW structure with a shallow
315 seismicity (Fig. 4a-b) and sum up in a total length of approximately 20 km. This rupture length is
316 confirmed by inverting synthetic aperture radar (SAR) data (Lin et al., 2015; Kobayashi et al., 2018).
317 The rupture length is likely greater than the expected for a M_w 6-6.2 (we estimated 8 km in total from
318 the rupture directivity analysis). This may be due (1) to the simple fault geometry that the code can
319 provide and (2) to the larger fault extent as imaged by the location of aftershock static-triggered at the
320 borders of the main rupture.

321 The final best rupture model (purple arrows in Fig. 4a) provides a fault rupture direction of N60° with
322 a total length of 8 km and a nearly pure bi-lateral evolution (e.g., equal predominant and secondary
323 rupture lengths of 4 km) at an average rupture velocity of 0.9β (with β as the S-wave velocity). We
324 note that the retrieved bi-lateral rupture mode and length match well the mainshock epicenter location
325 and the early-time (3 hours after MOT) spatial aftershock distribution. Moreover, the rupture
326 orientation derived from the mainshock directivity analysis, points toward South-West and North-East
327 which correspond well to the 1-3 km shallow and 4-6 km deep, high slip mainshock fault patch,
328 respectively (Kobayashi et al., 2018, see Fig. S15 in SM).

329 As from the aftershock distribution in the first 3 hours after the MOT, so during the first phase, the
330 seismicity deepens moving toward north-east (Fig. 4a-b and Fig. 5a,e,i,m), up to 8-9 km in the
331 northernmost sector (Fig. 5a). Moreover, the northern segment is more populated and characterized by
332 a small cluster activated by a major aftershock of M_{JMA} 4.4 at 4 km of depth during the first hour after
333 the MOT (green star in Fig. 4a-b and Fig. 5a). By considering the seismicity belonging to this cluster
334 in the entire time period (red dots in Fig. 4f and seismicity between 2 and 5 km of depth in Fig. 3 and
335 5d), we calculated the composite focal mechanism (cluster B in the Table S1 and Fig. S7) and found a
336 strike of 47°, dip 61° coherent with the main fault segment associated with the mainshock rupture and
337 the distribution of seismicity (Fig. 4f and Fig. 5a-d).

338 The south-western seismicity delineates a single fault plane which is coherent with the OTNF structure
339 (Fig. 4a-b and Fig. 5a-d; Panayotopoulos et al., 2016). In detail, the aftershocks delineate a fault

segment in the south of 8 km length with a strike of around 20° (Fig. 4a) and mainly up to 4 km of depth indicating that the mainshock ruptured upward (Fig. 5i). In previous works on the sequence (Panayotopoulos et al., 2016; Ando et al., 2017) there is almost no seismicity in the first two kilometers depth in the southernmost section compared to the locations obtained in this work (section A-A' on Fig. 4a-b and Fig. 5m). This discrepancy depends mostly on the difference of the catalog and on the use of the 3D velocity model that accounts for the strong lateral variation of velocity in this area characterized by two different domains (INZ and NFM in Fig. 1) placed side by side. This result is coherent with the slip release during the mainshock (Kobayashi et al., 2018), indeed the seismicity in the first 2 km of depth in the southernmost part of the sequence (Fig. 4a-b and Fig. 5m) is located at the edge of the high-slip patch of the mainshock at south around 1 km depth (Fig. S15 in SM). Coherently with this high-slip patch location, our locations show a clear gap in the south-west part of the southern segment (Fig. 4a-b, Panayotopoulos et al., 2016; Kobayashi et al., 2018).

By considering the seismicity clustered around the mainshock location in the entire period (magenta dots in Fig. 4f), we calculated the composite focal mechanism (cluster A in the Table S1 and Fig. S6) and found a fault plane with a strike of 20° and east-dipping of 55° which is coherent with the distribution in plane (Fig. 4f) and in depth (Fig. 3 and 5l) of clustered seismicity and with the mainshock CMT solution estimated by the NIED using F-net (NIED, 2014) (see Fig. 4a-b). For the shallow seismicity in the first two kilometers depth in the southernmost section A-A' (pink dots on Fig. 4f), we calculated the composite focal mechanism (cluster C in the Table S1 and Fig. S8) and found a fault plane with a strike of 20° and east-dipping of 50° which is coherent with the distribution in plane of the seismicity along fault segment in the southern part.

4.2. Phase 2 / Deep aftershocks distribution in the northern part

Between 12 and 24 hours after the MOT, in the northern part, in correspondence of the section C-C', a second major shock with M_{JMA} 4.4 occurred (green star in Fig. 4c and Fig. 5f) on a "new" segment. For the cluster associated with this major shock (black dots in Fig. 4f), we calculated the composite focal mechanism (cluster D in the Table S1 and Fig. S9) and we found a solution that gives a fault plane with a strike of 210° and west-dipping of 60° which is very coherent with the seismicity

distribution in depth (Fig. 5f). In the same time window, in the section D-D', the northernmost one, a significant increase of events is observed in the deep part (up to 8 km depth) of the northern sector (Fig. 5b).

After 24 hours from the MOT, we observed a significant increase of the number of events in the deeper part of the fault system, between 6 and 10 km of depth, starting from the northernmost section D-D' up to the section B-B' in the area of mainshock occurrence (Fig. 4d and Fig. 5c,g). However, it's not easy to define the activation time of the deep seismicity in the southern part. In section D-D' (Fig. 5c), we can distinguish two separate clusters, though very close, one between 6 and 8 km depth (blue dots in Fig. 4f) and the other, deeper, between 7 and 10 km (green dots in Fig. 4f). We calculated for these two clusters the composite focal mechanisms and found a CMT solution coherent in terms of strike and dip to the cluster distribution. The CMT solution of the cluster (cluster E in the Table S1 and Fig. S10) between 6 and 8 km of depth (blue dots in Fig. 4f) shows a fault plane with a strike of 70° and south-dipping of 80° and for the cluster (cluster F in the Table S1 and Fig. S11) between 7 and 10 km (green dots in Fig. 4f) the fault plane is striking 254° with a dip of 61° to the north. Moving toward south-west, in the section C-C' (Fig. 4d and Fig. 5g), it is clearly visible a cluster with a near-vertical distribution. For this cluster (cyan dots in Fig. 4f), we calculated the composite focal mechanism (cluster G in the Table S1 and Fig. S12) and found a strike of 206° and east-dipping of 77°, also in this case well matching the seismicity distributions. By considering the time delay of hours between cluster and main rupture occurrences, we can hypothesize the static stress transfer as the likely triggering mechanism.

In previous studies, the authors associated the deep seismicity in the northern part to the extension at depth of the mainshock related fault (Panayotopoulos et al., 2016; Ando et al., 2017). The small-scale complexity that we can reveal by considering high precision locations obtained refining the absolute picks, allowed us to identify and geometrically characterize these clusters. For each of them the estimated dominant focal mechanisms show sub-vertical planes coherent with the seismicity delineated fault.

4.3. Phase 3 / Deep aftershocks distribution in the southern part

One week after the MOT, also the depth portion (down to 3 km depth) of the southernmost part, in correspondence to the section A-A', is characterized by an increase of seismicity (Fig. 4e and Fig. 5p). We calculated the composite focal mechanism (cluster H in the Table S1 and Fig. S13) and found a fault plane solution with a strike of 16° and a dip of 77° to the east for the deep seismicity in the south part (yellow dots in Fig. 4f). For the seismicity between 2 and 4 km of depth (orange dots in Fig. 4f) the composite focal mechanism (cluster I in the Table S1 and Fig. S14) gives a fault plane with a strike of 20° and a dip of 80° to the east. By identifying the small-scale complexity of the southernmost part on the section A-A', we can distinguish the higher dipping structures of two southern segments with respect to the shallower part (cluster C on Fig. 4f and Fig. S8) and to the envelope of the seismicity which follows the dipping structure of the mainshock rupture with a dip of 55°. The gaps of aftershock at 6 km of depth in the northern part (red dashed contoured area in section C-C', Fig. 5h) and up to 2 km above the mainshock cluster (red dashed contoured area in section B-B', Fig. 5l) are well correlated with a high slip patch of the mainshock rupture (Kobayashi et al., 2018; see Fig. S15 in SM).

The shallower seismicity, down to 6 km depth, shows the occurrence of several relatively high magnitude shocks, followed by a power-decaying number of events with time from the mainshock (see Fig. 3 and S16 in SM). On the other hand, the deeper volume seems to have not been activated by major shocks and the temporal distribution of seismicity is almost constant in time (see Fig. S16 in SM). So, we can observe a different behavior in terms of seismicity time occurrence between the shallow and deep part of the fault system and between the northern and southern portion. This different behavior of cluster-events occurrence with time within the same seismic sequence has been already observed in other seismic regions worldwide and associated with different triggering mechanisms, static-stress transfer or pore-fluid induced effect (De Barros et al., 2019). Furthermore, this could also arise from the fact that some of the fault segments from the deep portion of the fault system are very steep, and therefore may not be optimally oriented to be (re)activated. However, further and more quantitative investigations are required to explain this observation.

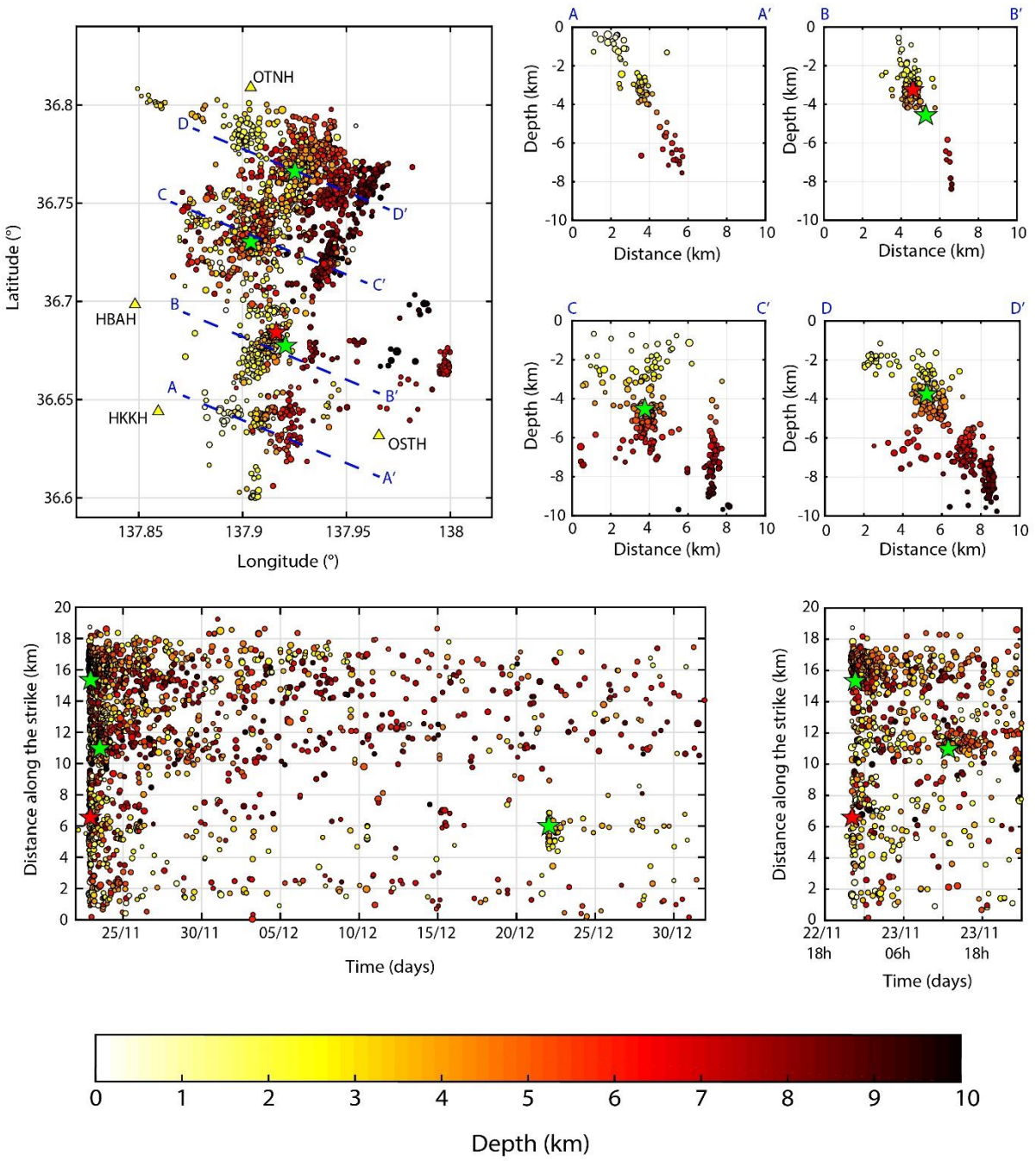

421

422 **Figure 3**. Map view, sections, and distribution of the seismicity along strike versus time
423 during the whole period of the earthquake sequence. Red star denotes the M_w 6.2 mainshock
424 and the green stars correspond to the major aftershock with a $M_{JMA} \geq 4$. Circles denote
425 aftershocks and sizes scale with magnitudes. Yellow triangles are the seismic stations. The
426 color bar indicates the depth. The blue dash lines indicate the position of the sections.

427

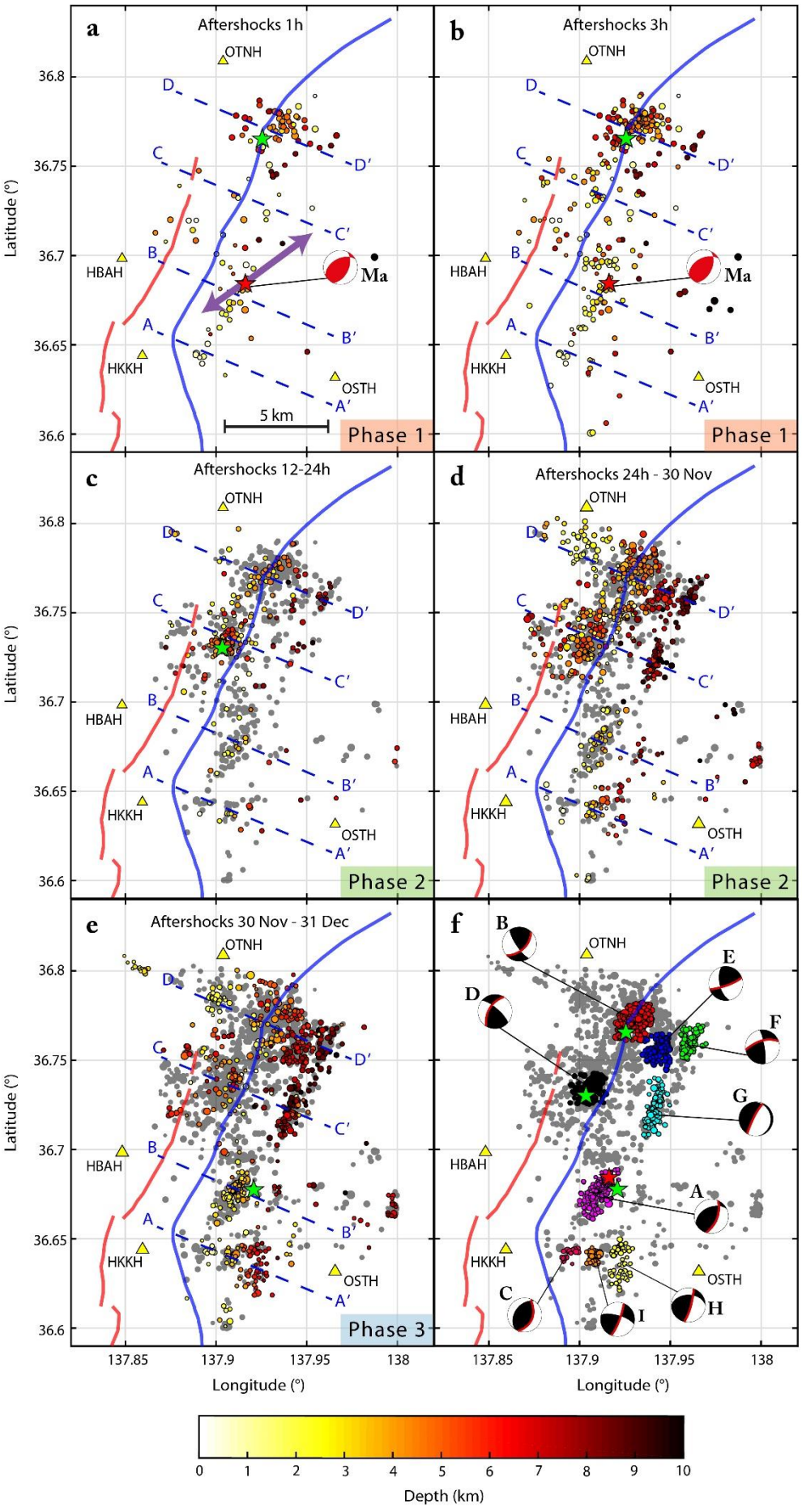
a
Aftershocks 1h
b
Aftershocks 3h
c
Aftershocks 12-24h
d
Aftershocks 24h - 30 Nov
e
Aftershocks 30 Nov - 31 Dec
f
OTNH
HBAH
HKKH
OSTH
A
A′
B
B′
C
C′
D
D′
Ma
5 km
Phase 1
Phase 2
Phase 3
Latitude (°)
Longitude (°)
Depth (km)

Figure 4. Spatial and temporal distribution of the aftershock sequence at different time periods after relocation (a-e) and the composite focal mechanism for each individual cluster (f). Red star denotes the mainshocks and the green stars correspond to the major aftershock with a $M_{JMA} \geq 4$. Circles denote aftershocks and sizes scale with magnitudes. Gray circles correspond to the aftershocks which occurred before the time interval. Yellow triangles are seismic stations. The color bar indicates the depth. The blue dash lines indicate the position of the sections. The focal mechanism represented in red is the CMT solution for the mainshock estimated by NIED using F-net. The red and blues lines on the map correspond to the fault traces at the surface of the Kamishiro fault and the Otari–Nakayama fault, respectively. The purple arrows indicate the rupture directivity and the rupture mode of the mainshock. The index letters of each composite focal mechanism are referred in the Table S1 in SM. The red line on the different focal mechanism corresponds to the related fault plane. The time periods are (see Table 1): a) from MOT to 1h after; b) from MOT to 3h after; c) from 12 to 24 h after MOT; d) from 24h to one week after MOT; e) from one week after the MOT to one month after MOT.

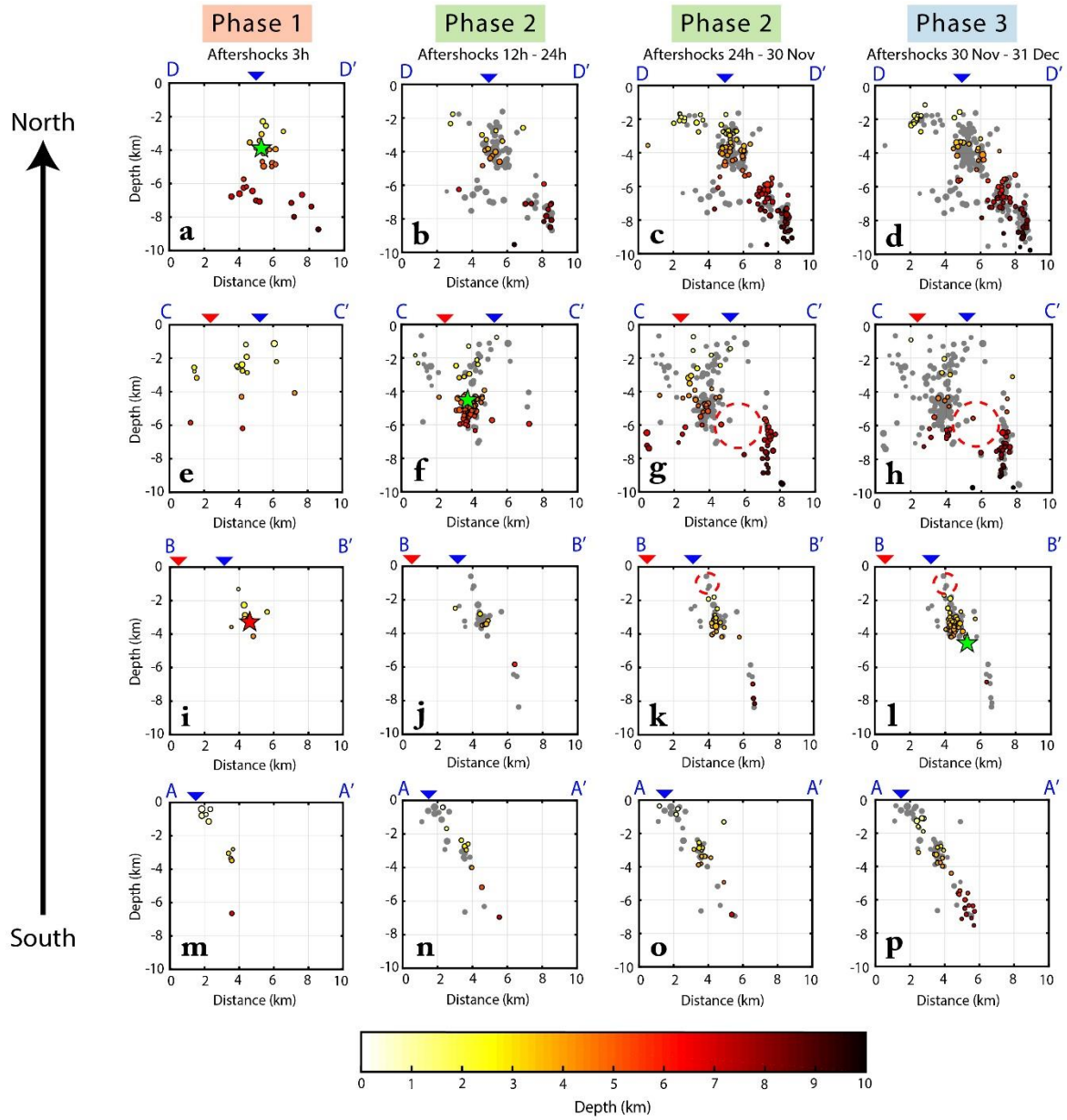

445

446 **Figure 5**. Cross-sections of the aftershocks sequence perpendicular to the fault's strike at
447 different time periods. Sections at depth at different time periods after the mainshock. Red
448 star denotes the mainshocks and the green stars correspond to the major aftershock with a
449 $M_{JMA} \geq 4$. Circles denote aftershocks and sizes scale with magnitudes. Gray circles
450 correspond to the aftershocks which occurred before the time interval. The color bar indicates
451 the depth. The red dash contours indicate the positions of the high slip patches from the model
452 estimated by Kobayashi et al., 2018.

5. 3D fault model and 4D rupture evolution

In this section we propose a 3D model of the segmented fault system and an evolutionary scenario of the sequence of activation of the various activated segments based on the spatial distribution of earthquakes together with the composite focal mechanisms of significant clusters.

5.1. 3D Segmented fault system

As previously mentioned, the fault zone responsible for the Nagano earthquake sequence is an inherited extensional fault which is currently being reactivated with a prevalent reverse kinematics in response to the inversion of the NFM basin. Although some characteristics of the original, extensional fault system such as the dip or strike of individual fault segments within it may be altered during fault inversion, the bulk 3D geometry (e.g., degree of fault segmentation, types of linkage between adjacent fault segments) is likely being preserved through the episode of fault reactivation.

Therefore, in describing and interpreting the 3D structure of the fault zone, it is reasonable to adopt geometrical templates and associated terminologies that have been used for extensional fault systems. It is well-known that extensional faults are in 3D seldom individual planar surfaces while are most often comprised of multiple fault segments (Walsh and Watterson, 1989; Childs et al., 1996, 2009; Peacock, 2002; Marchal et al., 2003; Walsh et al., 2003; Kristensen et al., 2008; Delogkos et al., 2017; Camanni et al., 2021, 2023b; Roche et al., 2021). An important notion to be introduced here is that of "relay zone", defined as the volume of rocks between two adjacent fault segments, whose deformation facilitates the transfer of displacement from one fault segment to another (Larsen, 1988; Peacock and Sanderson, 1991, 1994; Childs et al., 1995; Huggins et al., 1995; Camanni et al., 2019, 2023a,b; Delogkos et al., 2020; Mercuri et al., 2020 a,b; Nicol et al., 2020; Roche et al., 2020, 2021). In this work we are not concerned with the exact mechanism that acts across relay zones for transferring displacement, but rather of their 3D geometry. Therefore, in this section, we will first describe the 3D nature of the studied fault system, and we then compare it with other templates of 3D segmented normal fault surfaces described in the literature.

The southernmost fault segment is made up of a single, planar, east-dipping surface (segment A in Fig. 7, section B-B' in Fig. 6) which in the south splays in three, subordinate segments juxtaposed across two relay zones with a sub-horizontal axis (segments C-I-H in Fig. 7, section A-A' in Fig. 6). It is worth noting here that, in cross-section (panel b in Fig. 6), the envelopes of these three segments have a dip angle which is steeper to that of segment A (Fig. 6-7).

The northernmost fault segment is geometrically more articulated (Fig. 6-7). Overall, it is, in turn, comprised of two subordinate fault segments vertically juxtaposed across a relay zone, with a sub-horizontal relay axis; an antithetic fault (i.e., more prominently west-dipping) is associated with this relay zone (segment D in Fig. 7, section C-C' in Fig. 6). The upper segment (segment B in Fig. 6-7), is an individual east-dipping, surface, while the lower one is a sub-vertical to steeply west-dipping surface (segment G in Fig. 6-7) which is splaying in two minor segments (segments E and F in Fig. 6-7) towards the northern edge of the fault zone, which are juxtaposed against one another across a sub-horizontal, relay zone (section D-D' in Fig. 6).

The above-described 3D structure for the studied fault system derived from seismological observations has, geometrically, several characteristics in common with the 3D structure of normal faults as derived, in recent works, from fault mapping within datasets of higher resolution such as field and 3D seismic reflection ones (e.g., Marchal et al., 2003; Kristensen et al., 2008; Tvedt et al., 2013; Worthington and Walsh, 2017; Freitag et al., 2017; Lăpădat et al., 2017; Camanni et al., 2019; Roche et al., 2020, 2021). We stress that a direct comparison between datasets is viable since the segmentation of the fault studied here is interpreted to be inherited from an extensional fault. In particular, the most recent works among the ones cited above (e.g., Camanni et al., 2019; Roche et al., 2021) show that, overall, relay zones on normal faults are mostly either sub-horizontal (i.e., neutral relay zones) or sub-vertical (i.e., dip relay zones), and only secondarily oblique, in space, a characteristic in common with the fault zone studied in this work. Similarly, in circumstances in which a normal fault is vertically segmented, it has been shown that the individual fault segments have a sense of stepping which gives rise to mostly contractional rather than extensional strains in the relay zones between them (e.g., Camanni et al., 2019). This appears to be also valid for the fault zone

studied here, where the horizontally segmented faults have relay zones with a contractional geometrical configuration (see, e.g., relay zones between segments C-I-H, and relay zones between segments B-E-F). Finally, it is worth mentioning here that the resolution of the hypocenter data used in this study does not allow to define whether segments are connected or not from one another in space. However, for the sake of clarity, in Fig. 6-7 segments are drawn as physically disconnected. As we will see in the next section, though, all segments are part of a same, larger fault system.

5.2. 4D fault segment activation

The highly segmented nature of the Nagano earthquakes suggests that the rupture process during these events could be more of a cascading phenomenon than a single continuous rupture front propagating along a fault. Analysis of the temporal sequence of activation of the 3D segments previously described (Fig. 8b-e) within the time windows previously described, provide insights on the 4D evolution of the rupture activated during the 2014 Nagano earthquake sequence. The rupture directivity projected on the segmented fault system (Fig. 8a) follows the distribution of the higher slip patches along the fault. It is especially worth noting that the southern edge of the rupture directivity is associated with the shallowest and largest high slip patch, as well as with the surface rupture as previously described (Fig. 8a). During the first phase (Fig. 8b), the fault segments A-B-C are activated and show a sense of movement (Fig. 7) coherent with the orientation of the regional stress field. Segments A and C are showing a clear reverse sense of movement, while the segment B is showing a right lateral strike-slip sense of shear, likely due to the rotation of the fault toward the east in the northern part. These are also the segments that in 3D are aligned along the rupture directivity projected at depth, and it shows the link between the surface rupture in southern part (with high slip and low number of aftershock) and the segment B in the northern part (with low slip and high number of aftershock) within the main bilateral rupture. During the second phase (Fig. 8c), the seismicity seems to migrate northward and to be focused on the northern part of segment B and also migrate towards the deeper part of the fault system involving segments D-E-F-G located between 5 and 9 km depth, while segments I, F and the southern portion of segment B become inactive. Segments D, E, and F are showing a right lateral strike-slip sense of movement, while the segment G is showing a normal one. Finally, during the last

phase (Fig. 8d), in the south, there is a reactivation of southern mainshock segment A along with the activation of segments H and I while, in the north, only the deeper portion of the fault (i.e., segments E-F-G) remains active. Even if the segments H, I, and C are belonging the same fault envelope, the deeper segments H and I are showing a left lateral strike-slip sense of movement, while the segment C, activated during the mainshock rupture phase, shown a reverse kinematics. We can note the difference of the rupture mechanism of the segments among the later phases with respect to the ones of the first phase. This variation of the rupture mechanism can be explained by (i) a strong variation of the fault geometry with respect to the orientation of the regional stress field and (ii) the variation of the stress among the fault system in the days/weeks after stress release due to the mainshock rupture.

Overall, these results suggest that the initial structure of the segmented fault system has key controls not only on clustering earthquakes but also on the seismicity evolution during the first month aftershock occurrence and on the length of the earthquake rupture with straightforward repercussions on time-dependent seismic hazard changes.

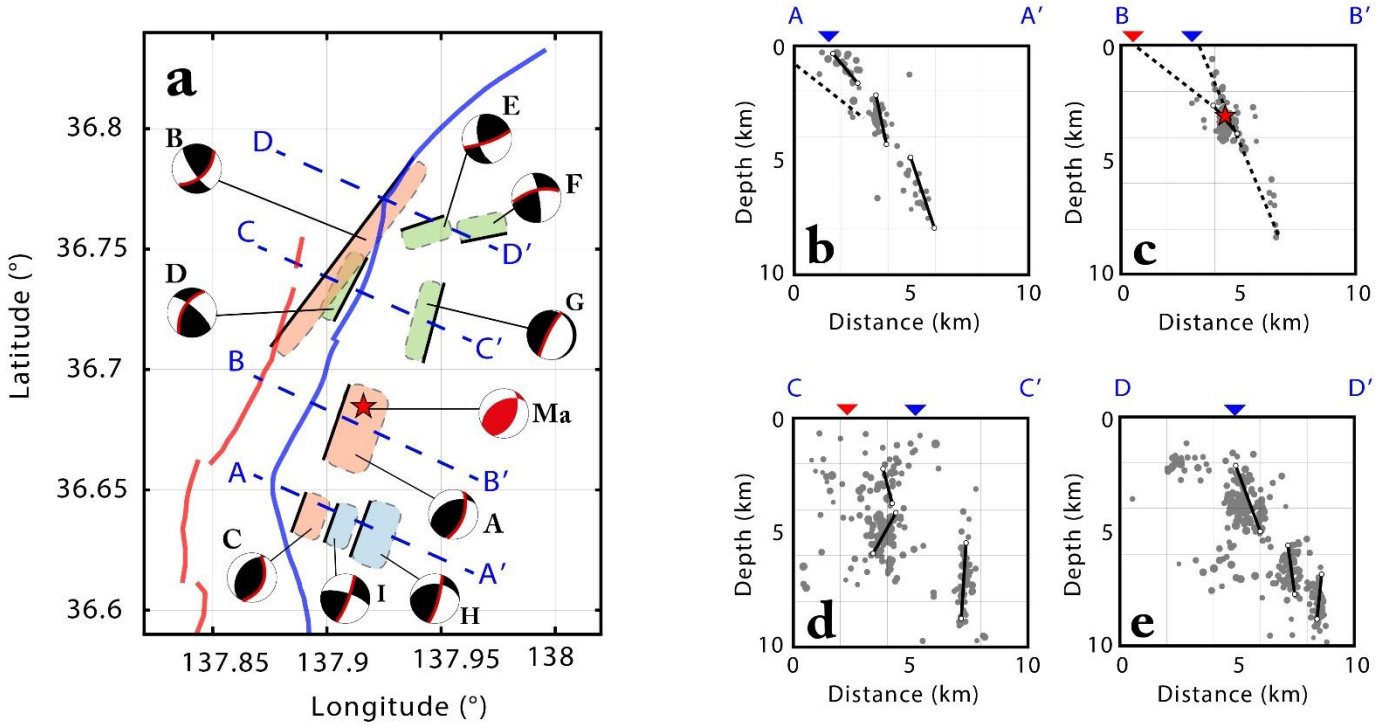

548

549

550 **Figure 6**. Map (a) and cross-section (b-e) views of the main fault segments identified in this
551 study. The color of the segment is following the 3 phases discussed in this study (orange: first
552 phase; green: second phase; blue: third phase). The index letters of each composite focal
553 mechanism are referred in the Table S1 in SM. The red and blues lines on the map correspond
554 to the fault traces at the surface of the Kamishiro fault and the Otari–Nakayama fault
555 respectively. The red and blue triangles on the sections correspond to the position of the fault
556 trace at the surface of the Kamishiro fault and the Otari–Nakayama fault respectively.

557

558

559

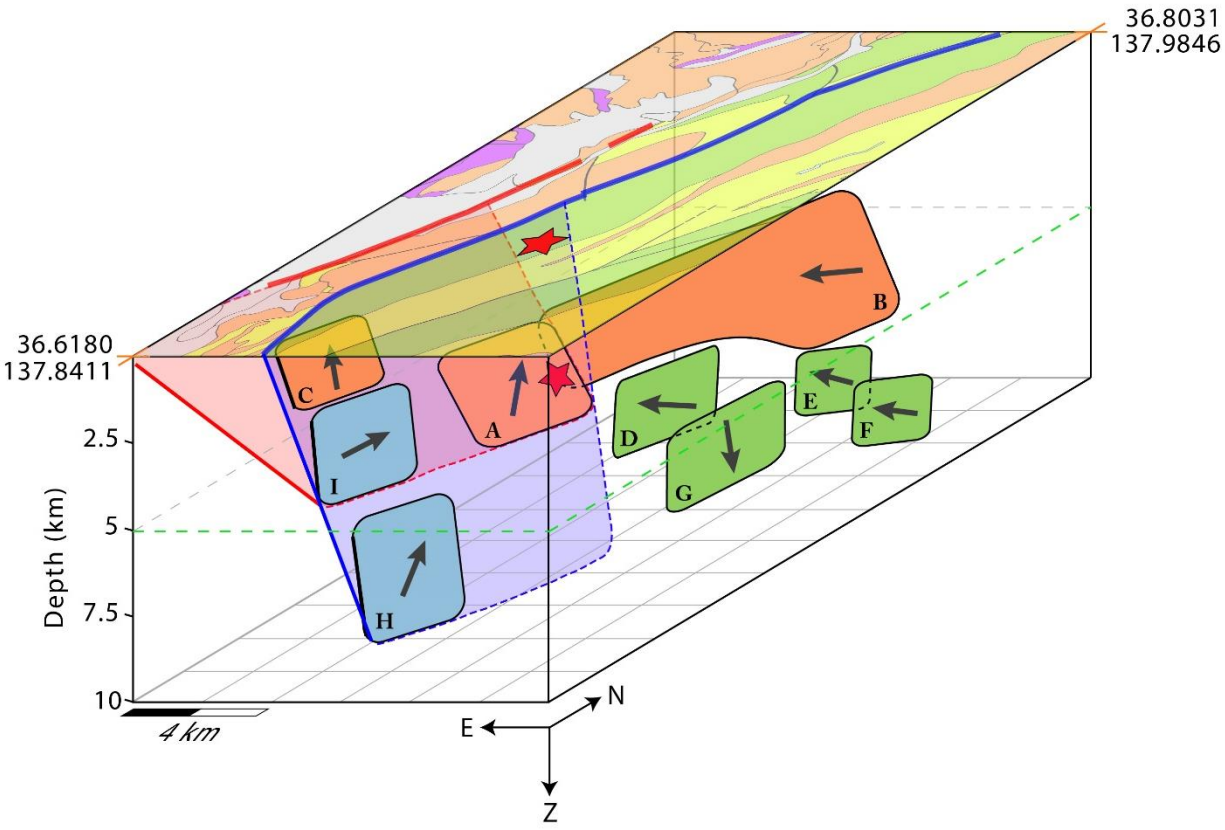

560 **Figure 7**. 3D model of the studied segmented fault system and geological map of the study
561 area (colors in the map are as in Fig. 1). The color of the segment is following the 3 phases
562 discussed in this study (orange: first phase; green: second phase; blue: third phase). The grey
563 arrows on the segments represent the movement on the fault with respect to the estimated
564 focal mechanisms. The index letters of each fault segment are referred in the Table S1 in SM.
565 The red and blues lines on the map correspond to the fault traces at the surface of the
566 Kamishiro fault and the Otari–Nakayama fault respectively. The red and blue surfaces at
567 depth correspond to the position of the fault plane of the Kamishiro fault and the Otari–
568 Nakayama fault respectively.

569

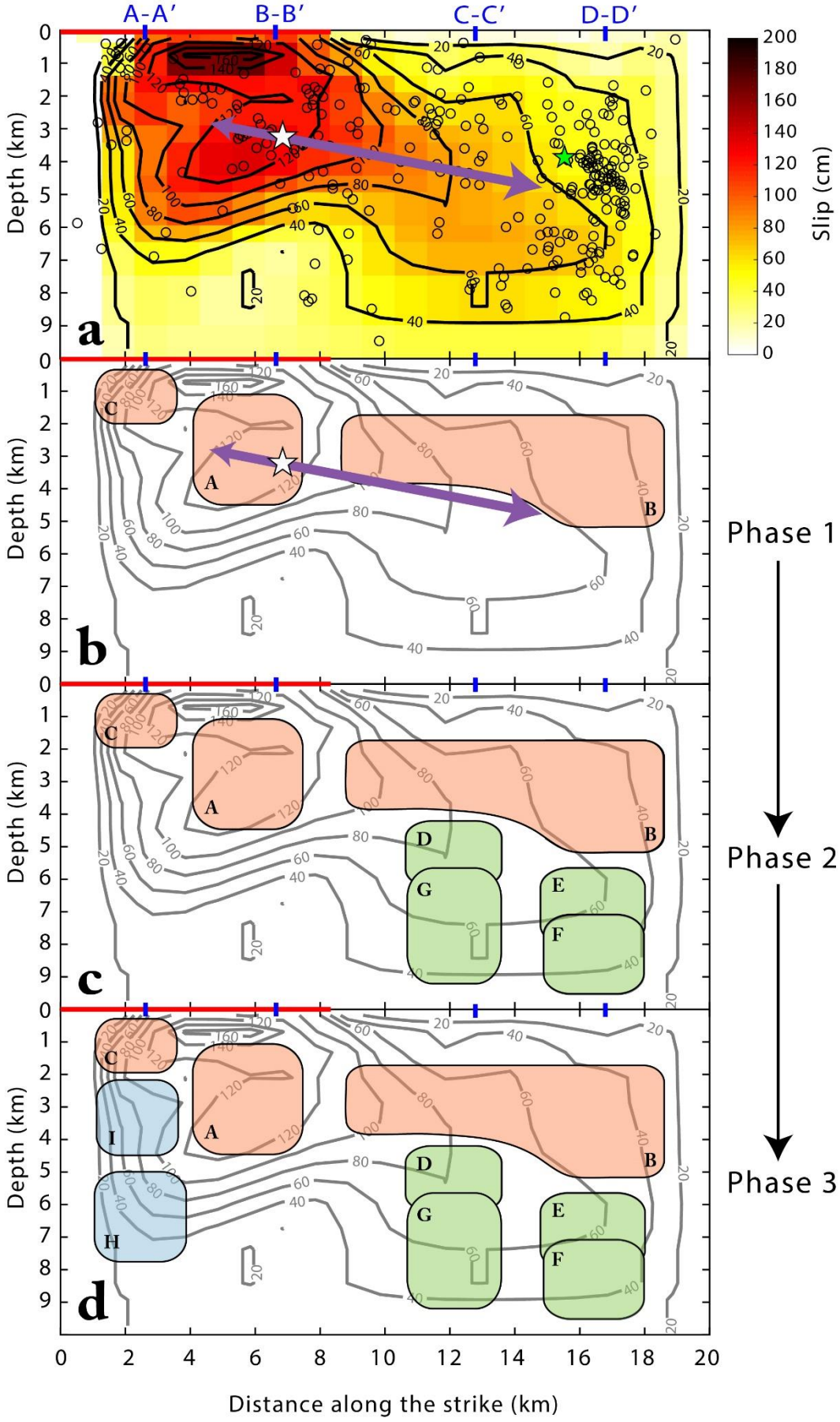
A-A′
B-B′
C-C′
D-D′
Depth (km)
Slip (cm)
200
180
160
140
120
100
80
60
40
20
0
a
b
c
d
A
B
C
D
E
F
G
H
I
Phase 1
Phase 2
Phase 3
Distance along the strike (km)
0
2
4
6
8
10
12
14
16
18
20

570

571 **Figure 8**. Fault strike-projection views of (a) the aftershock seismicity over the entire time
572 period on the slip model obtained by Kobayashi et al., 2018 and (b-e) the 4D seismicity
573 evolution of the Nagano earthquake sequence in the 3 phases described in this study. The
574 color of the segment is following the 3 phases. The index letters of each fault segment are
575 referred in the Table S1 in SM. Black circles indicate the aftershock location. White star
576 indicates the M_w 6.2 mainshock location. The gray lines indicate the contour of the slip along
577 the fault. The purple arrows indicate the rupture directivity and the rupture mode of the
578 mainshock. The red line indicates the position of the surface rupture.

579

580 **6. Conclusions**

581 With the aim to reconstruct the 3D multi-segmented rupture of the 2014 M_w 6.2 Nagano sequence, we
582 relocated the about 2500 aftershocks reconstructing an enhanced catalog with high-resolution
583 locations. In detail, we first enriched the JMA seismic catalog of the three months around the
584 mainshock by integrating around 10% of new events. Then, we constructed a new method for the
585 refinement of automatic picks that includes 1) the construction of family of co-located events with
586 high cross-correlation of waveforms at the same station; 2) the construction of a reference trace for
587 each family through a weighted stack of waveforms on which measure a reference automatic pick; 3)
588 the use of the reference pick to adjust the other picks of waveforms in the family. Each pick is
589 associated with a weight based on the SNR ratio around the refined pick. This procedure is crucial,
590 together with the use of reliable 3D velocity models, to obtain accurate depth estimations of events.
591 The refined picks were inverted by a tomographic approach to obtain 3D P- and S-wave velocity
592 models. We obtained the final location catalog by using the double-difference location method and 3D
593 velocity models (P and S-phase) optimized for the area.

594 The highly accurate relocation allowed us to unravel the 3D geometrical complexities of the fault
595 system by analyzing the spatial distribution of the aftershocks with unprecedented detail. The early
596 aftershock distribution and the strong motion data confirm the bilateral characteristic of the mainshock

rupture coherent with the distribution of aftershock in the first 3 hours after the mainshock occurrence. By following the aftershock evolution in time, a complex cascading rupture phenomena can be unraveled with the activation of 9 different fault segments well constrained in terms of geometry and activation time in 3D from seismicity and composite focal mechanisms data. The temporal evolution of fault activation into 3 phases involved first the shallow northern and southern portions, then the deeper northern portion of it and finally the deeper and the shallower part of the southern portion. Among the different fault segments, we observe a different behavior in terms of rupture triggering mechanisms depending on their spatial and temporal occurrence. This can be explained by a strong variation of the fault geometry with respect to the orientation of the regional stress field and the variation of the stress among the fault system in the days/weeks after stress release due to the mainshock rupture.

The proposed framework aimed to the reconstruction of the complexity of the fault system involved in the Mw 6.2, 2014 Nagano aftershock sequence can be used both to improve the hazard evaluation by including a more reliable source model, and, to suggest a similar, integrated approach applicable to other high-risk areas to obtain a more comprehensive image of fault complexity and time-changing hazard level related to the occurrence of moderate to large aftershock ruptures on mutual interacting fault segments.

Conflict of Interest

The authors declare that they have no known competing financial interests or personal relationships that could have appeared to influence the work reported in this paper.

Acknowledgments

The authors thank Vincenzo Convertito (INGV) for providing the code for rupture direction analysis and the support for its use. G. Camanni acknowledges members of the Fault Analysis Group of the

University College Dublin for many useful discussions on fault structure. This work has been supported by the PRIN-FLUIDS project: “Detection and tracking of crustal fluid by multi-parametric methodologies and technologies” of the Italian PRIN-MIUR program (Grant no.20174X3P29).

Data & Software Availability Statement

The continuous seismic records (Hi-net data) analyzed in this paper are available via https://doi.org/10.17598/NIED.0003. The strong motion data (KiK-net data) of the mainshock records are available from the National Research Institute of Earth Science and Disaster Resilience (https://www.doi.org/10.17598/NIED.0004). The absolute locations were processed by using the code NonLinLoc (http://www.alomax.net/nlloc). The composite focal mechanisms were computed using the code FPFIT (available on USGS via https://www.usgs.gov/software/fpfit-fpplot-and-fppage).

References

Adinolfi, G. M., Picozzi, M., Cesca, S., Heimann, S., & Zollo, A. (2020). An application of coherence-based method for earthquake detection and microseismic monitoring (Irpinia fault system, Southern Italy). Journal of Seismology, 24, 979-989.

Adinolfi, G. M., De Matteis, R., De Nardis, R., & Zollo, A. (2022). A functional tool to explore the reliability of micro-earthquake focal mechanism solutions for seismotectonic purposes. Solid Earth, 13(1), 65-83.

Adinolfi, G. M., De Landro, G., Picozzi, M., Carotenuto, F., Caruso, A., Nazeri, S., ... & Piantanida, M. (2023). Comprehensive study of micro-seismicity by using an automatic monitoring platform. *Frontiers in Earth Science*, *11*, 1073684.

Aki, K., & Richards, P. G. (2002). Quantitative seismology.

Akram, J., & Eaton, D. W. (2016). Refinement of arrival-time picks using a cross-correlation based workflow. *Journal of Applied Geophysics*, *135*, 55-66.

Amoroso, O., Napolitano, F., Hersir, G. P., Agustsdottir, T., Convertito, V., De Matteis, R., ... & Capuano, P. (2022). 3D seismic imaging of the Nesjavellir geothermal field, SW-Iceland. *Frontiers in Earth Science*, *10*, 994280.

649 Ando, R., Imanishi, K., Panayotopoulos, Y., & Kobayashi, T. (2017). Dynamic rupture propagation on
650 geometrically complex fault with along-strike variation of fault maturity: insights from the 2014
651 Northern Nagano earthquake. *Earth, Planets and Space*, *69*(1), 1-13.
652 Asano, Y., Saito, T., Ito, Y., Shiomi, K., Hirose, H., Matsumoto, T., Hiro, S., & Sekiguchi, S. (2011). Spatial
653 distribution and focal mechanisms of aftershocks of the 2011 off the Pacific coast of Tohoku
654 Earthquake. *Earth, planets and space*, *63*(7), 669-673.
655 Baillard, C., Crawford, W. C., Ballu, V., Hibert, C., & Mangeney, A. (2014). An automatic kurtosis-based P-and
656 S-phase picker designed for local seismic networks. *Bulletin of the Seismological Society of*
657 *America*, *104*(1), 394-409.
658 Boatwright, J. (2007). The persistence of directivity in small earthquakes. *Bulletin of the Seismological Society*
659 *of America*, 97(6), 1850-1861
660 Camanni, G., Roche, V., Childs, C., Manzocchi, T., Walsh, J., Conneally, J., ... & Delogkos, E. (2019). The
661 three-dimensional geometry of relay zones within segmented normal faults. *Journal of Structural*
662 *Geology*, *129*, 103895.
663 Camanni, G., Vinci, F., Tavani, S., Ferrandino, V., Mazzoli, S., Corradetti, A., ... & Iannace, A. (2021). Fracture
664 density variations within a reservoir-scale normal fault zone: a case study from shallow-water
665 carbonates of southern Italy. *Journal of Structural Geology*, *151*, 104432.
666 Camanni, G., Childs, C., Delogkos, E., Roche, V., Manzocchi, T., & Walsh, J. (2023a). The role of antithetic
667 faults in transferring displacement across contractional relay zones on normal faults. *Journal of*
668 *Structural Geology*, *168*, 104827.
669 Camanni, G., Freda, G., Delogkos, E., Nicol, A., & Childs, C. (2023b). 3D geometry and displacement transfer
670 of an oblique relay zone on outcropping normal faults. *Journal of Structural Geology*, *177*, 105001.
671 Cesca, S., Zhang, Y., Mouslopoulou, V., Wang, R., Saul, J., Savage, M., ... & Dahm, T. (2017). Complex rupture
672 process of the Mw 7.8, 2016, Kaikoura earthquake, New Zealand, and its aftershock sequence. *Earth*
673 *and Planetary Science Letters*, *478*, 110-120.
674 Chiaraluce, L., Ellsworth, W. L., Chiarabba, C., & Cocco, M. (2003). Imaging the complexity of an active
675 normal fault system: The 1997 Colfiorito (central Italy) case study. *Journal of Geophysical Research:*
676 *Solid Earth*, 108(B6).
677 Childs, C., Watterson, J., & Walsh, J. J. (1995). Fault overlap zones within developing normal fault
678 systems. *Journal of the Geological Society*, 152(3), 535-549.

679 Childs, C., Nicol, A., Walsh, J. J., Watterson, J. (1996). Growth of vertically segmented normal faults. *Journal of*
680 *Structural Geology*, 18, 1389-1397.
681 Childs, C., Manzocchi, T., Walsh, J. J., Bonson, C. G., Nicol, A., & Schöpfer, M. P. (2009). A geometric model
682 of fault zone and fault rock thickness variations. *Journal of Structural Geology*, 31(2), 117-127.
683 Convertito, V., Caccavale, M., De Matteis, R., Emolo, A., Wald, D., & Zollo, A. (2012). Fault extent estimation
684 for near-real-time ground-shaking map computation purposes. *Bulletin of the Seismological Society of*
685 *America*, *102*(2), 661-679.
686 Delogkos, E., Manzocchi, T., Childs, C., Sachanidis, C., Barbas, T., Schöpfer, M. P., ... & Walsh, J. J. (2017).
687 Throw partitioning across normal fault zones in the Ptolemais Basin, Greece. *Geological Society,*
688 *London, Special Publications*, 439(1), 333-353.
689 Delogkos, E., Manzocchi, T., Childs, C., Camanni, G., & Roche, V. (2020). The 3D structure of a normal fault
690 from multiple outcrop observations. *Journal of Structural Geology*, *136*, 104009.
691 De Barros, L., Baques, M., Godano, M., Helmstetter, A., Deschamps, A., Larroque, C., & Courboulex, F. (2019).
692 Fluid-induced swarms and coseismic stress transfer: A dual process highlighted in the aftershock
693 sequence of the 7 April 2014 earthquake (Ml 4.8, Ubaye, France). *Journal of Geophysical Research:*
694 *Solid Earth*, *124*(4), 3918-3932.
695 De Landro, G., Amoroso, O., Russo, G., & Zollo, A. (2020). 4d travel-time tomography as a tool for tracking
696 fluid-driven medium changes in offshore oil–gas exploitation areas. *Energies*, *13*(22), 5878.
697 De Landro, G., Amoroso, O., Russo, G., D'Agostino, N., Esposito, R., Emolo, A., & Zollo, A. (2022). Decade-
698 long monitoring of seismic velocity changes at the Irpinia fault system (southern Italy) reveals pore
699 pressure pulsations. *Scientific Reports*, *12*(1), 1247.
700 Freitag, U. A., Sanderson, D. J., Lonergan, L., & Bevan, T. G. (2017). Comparison of upwards splaying and
701 upwards merging segmented normal faults. *Journal of Structural Geology*, 100, 1-11.
702 Hamling, I. J., Hreinsdóttir, S., Clark, K., Elliott, J., Liang, C., Fielding, E., ... & Stirling, M. (2017). Complex
703 multifault rupture during the 2016 M w 7.8 Kaikōura earthquake, New Zealand. *Science*, *356*(6334),
704 eaam7194.
705 Hauksson, E., & Shearer, P. M. (2006). Attenuation models (QP and QS) in three dimensions of the southern
706 California crust: Inferred fluid saturation at seismogenic depths. *Journal of Geophysical Research:*
707 *Solid Earth*, 111(B5).

Heimann, S., Kriegerowski, M., Isken, M., Cesca, S., Daout, S., Grigoli, F., Juretzek, C., Megies, T., Nooshiri, N., Steinberg, A., Sudhaus, H., Vasyura-Bathke, H., Willey, T., Dahm, T., (2017). Pyrocko - An open-source seismology toolbox and library. Potsdam: GFZ Data Services. https://doi.org/10.5880/GFZ.2.1.2017.001

Hirata, N., Ohmi, S., Sakai, S. I., Katsumata, K., Matsumoto, S., Takanami, T., ... & Shimizu, H. (1996). Urgent joint observation of aftershocks of the 1995 Hyogo-ken Nanbu earthquake. *Journal of Physics of the Earth*, *44*(4), 317-328.

Huggins, P., Watterson, J., Walsh, J. J., & Childs, C. (1995). Relay zone geometry and displacement transfer between normal faults recorded in coal-mine plans. *Journal of Structural Geology*, 17(12), 1741-1755.

Iacoletti, S., Cremen, G. and Galasso, C., 2021. Advancements in multi-rupture time-dependent seismic hazard modeling, including fault interaction. *Earth-Science Reviews*, *220*, p.103650.

Imanishi, K., & Uchide, T. (2017). Non-self-similar source property for microforeshocks of the 2014 Mw 6.2 Northern Nagano, central Japan, earthquake. *Geophysical Research Letters*, *44*(11), 5401-5410.

Improta, L., Latorre, D., Margheriti, L., Nardi, A., Marchetti, A., Lombardi, A. M., ... & Moretti, M. (2019). Multi-segment rupture of the 2016 Amatrice-Visso-Norcia seismic sequence (central Italy) constrained by the first high-quality catalog of Early Aftershocks. *Scientific Reports*, *9*(1), 6921.

Japan Meteorological Agency, 2014. Monthly report on earthquakes and volcanoes in Japan, November 2014. http://www.data.jma.go.jp/svd/eqev/data/gaikyo/monthly/201411/201411monthly.pdf.

Kanno, T., Narita, A., Morikawa, N., Fujiwara, H., & Fukushima, Y. (2006). A new attenuation relation for strong ground motion in Japan based on recorded data. *Bulletin of the Seismological Society of America*, 96(3), 879-897.

Kano, K., Kosaka, K., Murata, A., & Yanai, S. (1990). Intra-arc deformations with vertical rotation axes: the case of the pre-Middle Miocene terranes of Southwest Japan. *Tectonophysics*, 176(3-4), 333-354.

Karabacak, V., Özkaymak, Ç., Sözbilir, H., Tatar, O., Aktuğ, B., Cevdet Özdağ, Ö., Çakir, R., Aksoy, E., Koçbulut, F., Softa, M., Akgün, E., Demir, A., Arslan, G. (2023). The 2023 Pazarcık (Kahramanmaraş, Türkiye) earthquake (Mw 7.7): Implications for surface rupture dynamics along the East Anatolian fault zone. *Journal of the Geological Society*, *180*(3), jgs2023-020.

Kato, H. (1992). FOSSA MAGMA-A masked border region separating southwest and northeast Japan.

Kobayashi, T., Morishita, Y., & Yarai, H. (2018). SAR-revealed slip partitioning on a bending fault plane for the 2014 Northern Nagano earthquake at the northern Itoigawa–Shizuoka tectonic line. *Tectonophysics*, *733*, 85-99.

Kristensen, M. B., Childs, C. J., & Korstgård, J. A. (2008). The 3D geometry of small-scale relay zones between normal faults in soft sediments. *Journal of Structural Geology*, 30(2), 257-272.

Lăpădat, A., Imber, J., Yielding, G., Iacopini, D., McCaffrey, K. J., Long, J. J., Jones, R. R., 2017. Occurrence and development of folding related to normal faulting within a mechanically heterogeneous sedimentary sequence: a case study from Inner Moray Firth, UK. *Geological Society*, London, Special Publications 439, 373-394.

Larsen, P. H. (1988). Relay structures in a Lower Permian basement-involved extension system, East Greenland. *Journal of Structural Geology*, 10(1), 3-8.

Latorre, D., Virieux, J., Monfret, T., Monteiller, V., Vanorio, T., Got, J. L., & Lyon-Caen, H. (2004). A new seismic tomography of Aigion area (Gulf of Corinth, Greece) from the 1991 data set. *Geophysical Journal International*, *159*(3), 1013-1031.

Lin, A., Ren, Z., Jia, D., & Wu, X. (2009). Co-seismic thrusting rupture and slip distribution produced by the 2008 Mw 7.9 Wenchuan earthquake, China. *Tectonophysics*, *471*(3-4), 203-215.

Lin, A., Sano, M., Yan, B., & Wang, M. (2015). Co-seismic surface ruptures produced by the 2014 Mw 6.2 Nagano earthquake, along the Itoigawa–Shizuoka tectonic line, central Japan. *Tectonophysics*, 656, 142-153.

Lois, A., E. Sokos, N. Maratakis, P. Paraskevopoulos, and G. A. Tselentis, 2013, A new automatic S-onset detection technique: Application in local earthquake data: Geophysics, 78, no. 1, KS1–KS11, doi:10.1190/geo2012-0050.1

Lomax, A., Michelini, A., Curtis, A., & Meyers, R. A. (2009). Earthquake location, direct, global-search methods. *Encyclopedia of complexity and systems science*, *5*, 2449-2473.

Manighetti, I., Campillo, M., Bouley, S., & Cotton, F. (2007). Earthquake scaling, fault segmentation, and structural maturity. *Earth and Planetary Science Letters*, 253(3–4), 429–438.

Manighetti, I., Zigone, D., Campillo, M., & Cotton, F. (2009). Self-similarity of the largest-scale segmentation of the faults: Implications for earthquake behavior. *Earth and Planetary Science Letters*, *288*(3-4), 370-381.

765 Marchal, D., Guiraud, M., & Rives, T. (2003). Geometric and morphologic evolution of normal fault planes and
766 traces from 2D to 4D data. *Journal of Structural geology*, 25(1), 135-158.
767 Matsuta, N., Ikeda, Y., & Sato, H. (2004). The slip-rate along the northern Itoigawa-Shizuoka tectonic line active
768 fault system, central Japan. *Earth, planets and space*, *56*(12), 1323-1330.
769 Mercuri, M., McCaffrey, K. J., Smeraglia, L., Mazzanti, P., Collettini, C., & Carminati, E. (2020a). Complex
770 geometry and kinematics of subsidiary faults within a carbonate-hosted relay ramp. *Journal of*
771 *Structural Geology*, 130, 103915.
772 Mercuri, M., Carminati, E., Tartarello, M. C., Brandano, M., Mazzanti, P., Brunetti, A., ... & Collettini, C.
773 (2020b). Lithological and structural control on fracture frequency distribution within a carbonate-hosted
774 relay ramp. *Journal of Structural Geology*, 137, 104085.
775 Michele, M., Chiaraluce, L., Di Stefano, R., & Waldhauser, F. (2020). Fine-scale structure of the 2016–2017
776 Central Italy seismic sequence from data recorded at the Italian National Network. *Journal of*
777 *Geophysical Research: Solid Earth*, *125*(4), e2019JB018440.
778 National Research Institute for Earth Science and Disaster Prevention, 2014. NIED seismic moment tensor
779 catalogue. National Research Institute for Earth Science and Disaster Prevention. (available online
780 from: http://www.fnet.bosai.go.jp/event/joho.php? LANG=en).
781 National Research Institute for Earth Science and Disaster Resilience (2019), NIED K-NET, KiK-net, National
782 Research Institute for Earth Science and Disaster Resilience, doi:10.17598/NIED.0004
783 Nicol, A., Gillespie, P. A., Childs, C., & Walsh, J. J. (2002). Relay zones between mesoscopic thrust faults in
784 layered sedimentary sequences. *Journal of Structural Geology*, *24*(4), 709-727.
785 Nicol, A., Walsh, J., Childs, C., & Manzocchi, T. (2020). The growth of faults. In Understanding faults (pp. 221-
786 255). *Elsevier*.
787 Okada, S., Ishimura, D., Niwa, Y., & Toda, S. (2015). The First Surface-Rupturing Earthquake in 20 Years on a
788 HERP Active Fault is Not Characteristic: The 2014 Mw 6.2 Nagano Event along the Northern
789 Itoigawa–Shizuoka Tectonic Line. *Seismological Research Letters*, *86*(5), 1287-1300.
790 Otofuji, Y. I., Matsuda, T., & Nohda, S. (1985). Paleomagnetic evidence for the Miocene counter-clockwise
791 rotation of Northeast Japan—rifting process of the Japan Arc. *Earth and Planetary Science*
792 *Letters*, 75(2-3), 265-277.
793 Özkan, A., Solak, H., I., Tiryakioğlu, I., Şentürk, M., D., Aktuğ, B., Gezgin, C., Poyraz, F., Duman, H., Masson,
794 F., Uslular, G., Yiğit, C., O., Yavaşoğlu, H. H. (2023). Characterization of the co-seismic pattern and

slip distribution of the February 06, 2023, Kahramanmaraş (Turkey) earthquakes (Mw 7.7 and Mw 7.6) with a dense GNSS network. *Tectonophysics*, *866*, 230041.

Panayotopoulos, Y., Hirata, N., Sato, H., Kato, A., Imanishi, K., Kuwahara, Y., Cho, I., Takeda, T. & Asano, Y. (2013). Investigating the role of the Itoigawa-Shizuoka tectonic line towards the evolution of the Northern Fossa Magna rift basin. *Tectonophysics*, *615*, 12-26.

Panayotopoulos, Y., Hirata, N., Hashima, A., Iwasaki, T., Sakai, S. I., & Sato, H. (2016). Seismological evidence of an active footwall shortcut thrust in the Northern Itoigawa–Shizuoka Tectonic Line derived by the aftershock sequence of the 2014 M 6.7 Northern Nagano earthquake. *Tectonophysics*, *679*, 15-28.

Peacock, D. C. P., & Sanderson, D. J. (1991). Displacements, segment linkage and relay ramps in normal fault zones. *Journal of Structural Geology*, 13(6), 721-733.

Peacock, D. C. P. (2002). Propagation, interaction and linkage in normal fault systems. *Earth-Science Reviews*, 58(1-2), 121-142.

Petersen, G. M., Büyükakpinar, P., Vera Sanhueza, F. O., Metz, M., Cesca, S., Akbayram, K., Saul, J., & Dahm, T. (2023). The 2023 Southeast Türkiye seismic sequence: rupture of a complex fault network. *The Seismic Record*, *3*(2), 134-143.

Reasenberg, P. A. (1985). FPFIT, FPPLOT, and FPPAGE: Fortran computer programs for calculating and displaying earthquake fault-plane solutions. *US Geol. Surv. Open-File Rep.*, 85-739.

Reitman, N. G., Briggs, R. W., Barnhart, W. D., Hatem, A. E., Thompson Jobe, J. A., DuRoss, C. B., Gold, R., C., Mejstrik, J., D., Collett, C., Koehler, R., D., & Akçiz, S. (2023). Rapid surface rupture mapping from satellite data: The 2023 Kahramanmaraş, Turkey (Türkiye), earthquake sequence. *The Seismic Record*, *3*(4), 289-298.

Roche, V., Childs, C., Madritsch, H., & Camanni, G. (2020). Layering and structural inheritance controls on fault zone structure in three dimensions: A case study from the northern Molasse Basin, Switzerland. *Journal of the Geological Society*, *177*(3), 493-508.

Roche, V., Camanni, G., Childs, C., Manzocchi, T., Walsh, J., Conneally, J., ... & Delogkos, E. (2021). Variability in the three-dimensional geometry of segmented normal fault surfaces. *Earth-Science Reviews*, *216*, 103523.

Roche, V., van der Baan, M., & Walsh, J. (2022, November). Examples of fault steps controlling event migration in seismic swarms. In *SEG International Exposition and Annual Meeting* (p. D011S168R002). SEG.

824 Ross, Z. E., & Ben-Zion, Y. (2014). Automatic picking of direct P, S seismic phases and fault zone head
825 waves. *Geophysical Journal International*, *199*(1), 368-381.
826 Ross, Z. E., Idini, B., Jia, Z., Stephenson, O. L., Zhong, M., Wang, X., ... & Jung, J. (2019). Hierarchical
827 interlocked orthogonal faulting in the 2019 Ridgecrest earthquake sequence. *Science*, *366*(6463), 346-
828 351.
829 Sato, H. (1994). The relationship between late Cenozoic tectonic events and stress field and basin development
830 in northeast Japan. *Journal of Geophysical Research: Solid Earth*, *99*(B11), 22261-22274.
831 Sato, H. (1996). Inversion tectonics of Japanese Islands. *Active Fault Res*, *15*, 128-132.
832 Sato, H., Iwasaki, T., Kawasaki, S., Ikeda, Y., Matsuta, N., Takeda, T., ... & Kawanaka, T. (2004). Formation
833 and shortening deformation of a back-arc rift basin revealed by deep seismic profiling, central
834 Japan. *Tectonophysics*, *388*(1-4), 47-58.
835 Taira, A. (2001). Tectonic evolution of the Japanese island arc system. *Annual Review of Earth and Planetary*
836 *Sciences*, *29*(1), 109-134.
837 Takano, O. (2002). Changes in depositional systems and sequences in response to basin evolution in a rifted and
838 inverted basin: an example from the Neogene Niigata-Shin'etsu basin, Northern Fossa Magna, central
839 Japan. *Sedimentary Geology*, *152*(1-2), 79-97.
840 Takeda, T., Sato, H., Iwasaki, T., Matsuta, N., Sakai, S. I., Iidaka, T., & Kato, A. (2004). Crustal structure in the
841 northern Fossa Magna region, central Japan, modeled from refraction/wide-angle reflection data. *Earth,*
842 *planets and space*, *56*, 1293-1299.
843 Toker, M., Yavuz, E., Utkucu, M., & Uzunca, F. (2023). Multiple segmentation and seismogenic evolution of
844 the 6th February 2023 (Mw 7.8 and 7.7) consecutive earthquake ruptures and aftershock deformation in
845 the Maras triple junction region of SE-Anatolia, Turkey. *Physics of the Earth and Planetary*
846 *Interiors*, *345*, 107114.
847 Tondi, E., Jablonská, D., Volatili, T., Michele, M., Mazzoli, S., Pierantoni, P. P. (2020), The Campotosto linkage
848 fault zone between the 2009 and 2016 seismic sequences of central Italy: Implications for seismic
849 hazard analysis. *GSA Bulletin*; 133 (7-8): 1679–1694. doi: https://doi.org/10.1130/B35788.1
850 Tvedt, A. B., Rotevatn, A., Jackson, C. A. L., Fossen, H., & Gawthorpe, R. L. (2013). Growth of normal faults in
851 multilayer sequences: A 3D seismic case study from the Egersund Basin, Norwegian North
852 Sea. *Journal of Structural Geology*, 55, 1-20.

Ulrich, T., Gabriel, A. A., Ampuero, J. P., & Xu, W. (2019). Dynamic viability of the 2016 Mw 7.8 Kaikōura earthquake cascade on weak crustal faults. *Nature communications*, *10*(1), 1213.

Valoroso, L., Chiaraluce, L., & Collettini, C. (2014). Earthquakes and fault zone structure. *Geology*, 42(4), 343-346.

Waldhauser, F., & Ellsworth, W. L. (2000). A double-difference earthquake location algorithm: Method and application to the northern Hayward fault, California. *Bulletin of the seismological society of America*, *90*(6), 1353-1368.

Waldhauser, F., Michele, M., Chiaraluce, L., Di Stefano, R., & Schaff, D. P. (2021). Fault planes, fault zone structure and detachment fragmentation resolved with high-precision aftershock locations of the 2016-2017 central Italy sequence. Geophysical Research Letters, 48, e2021GL092918. https://doi.org/10.1029/2021GL092918

Walsh, J. J., & Watterson, J. (1989). Displacement gradients on fault surfaces. *Journal of Structural Geology*, 11(3), 307-316.

Walsh, J. J., Bailey, W. R., Childs, C., Nicol, A., & Bonson, C. G. (2003). Formation of segmented normal faults: a 3-D perspective. *Journal of Structural Geology*, *25*(8), 1251-1262.

Wesnousky, S. G. (1988). Seismological and structural evolution of strike-slip faults. *Nature*, *335*(6188), 340-343.

Wesnousky, S. G. (2006). Predicting the endpoints of earthquake ruptures. *Nature*, *444*(7117), 358-360.

Williams, G. D., Powell, C. M., & Cooper, M. A. (1989). Geometry and kinematics of inversion tectonics. *Geological Society, London, Special Publications*, 44(1), 3-15.

Worthington, R. P., & Walsh, J. J. (2017). Timing, growth and structure of a reactivated basin-bounding fault. *Geological Society, London, Special Publications*, 439(1), 511-531.

Yamaji, A. (1990). Rapid intra-arc rifting in Miocene northeast Japan. *Tectonics*, *9*(3), 365-378.

Zollo, A., Caruso, A., De Landro, G., Colombelli, S., & Elia, L. (2021). A Bayesian Method for Real-Time Earthquake Location Using Multiparameter Data. *Journal of Geophysical Research: Solid Earth*, *126*(3), e2020JB020359.

Figure 1.

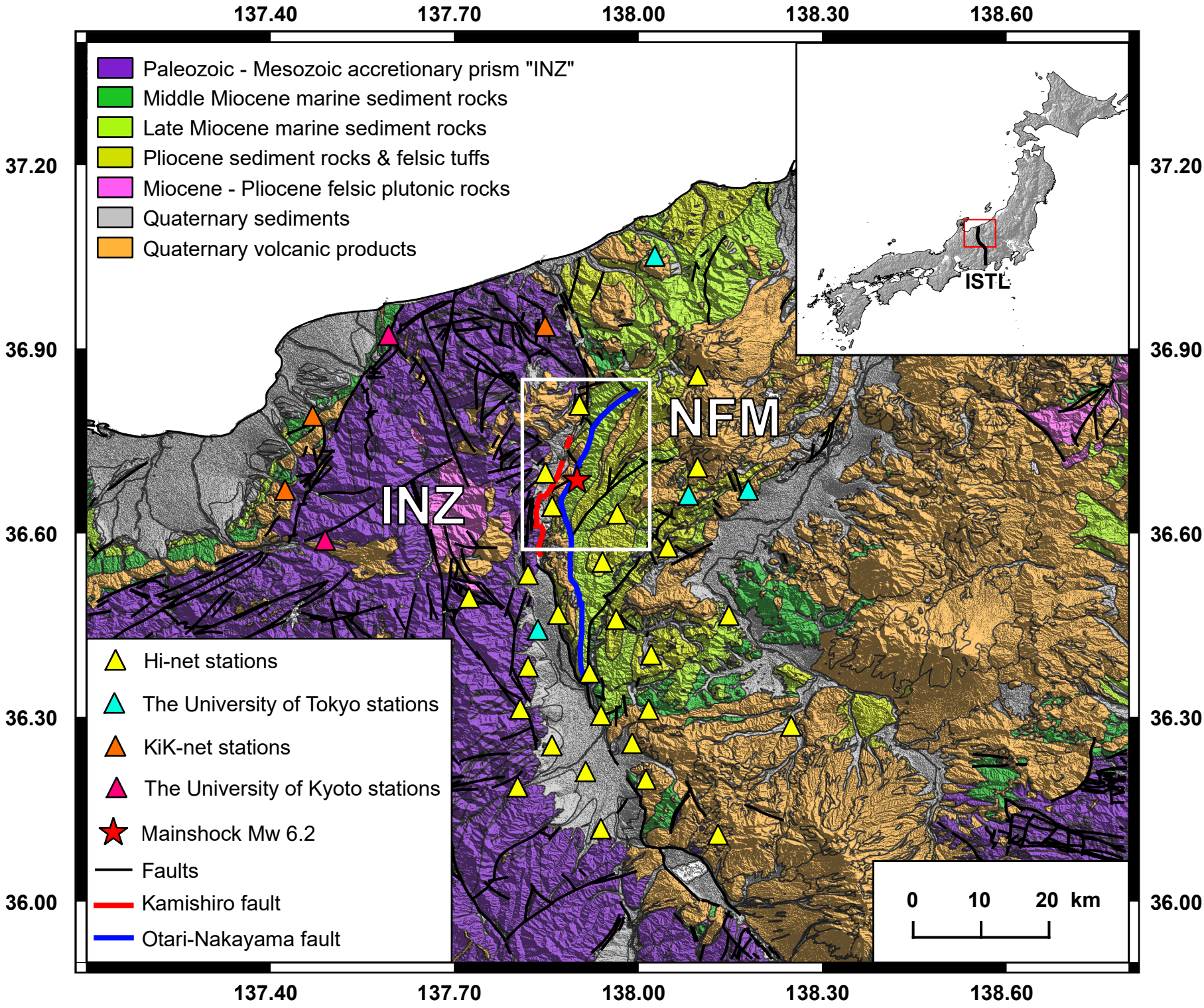
137.40
137.70
138.00
138.30
138.60
37.20
36.90
36.60
36.30
36.00
Paleozoic - Mesozoic accretionary prism "INZ"
Middle Miocene marine sediment rocks
Late Miocene marine sediment rocks
Pliocene sediment rocks & felsic tuffs
Miocene - Pliocene felsic plutonic rocks
Quaternary sediments
Quaternary volcanic products
ISTL
INZ
NFM
Hi-net stations
The University of Tokyo stations
KiK-net stations
The University of Kyoto stations
Mainshock Mw 6.2
Faults
Kamishiro fault
Otari-Nakayama fault
0
10
20 km

Figure 2.

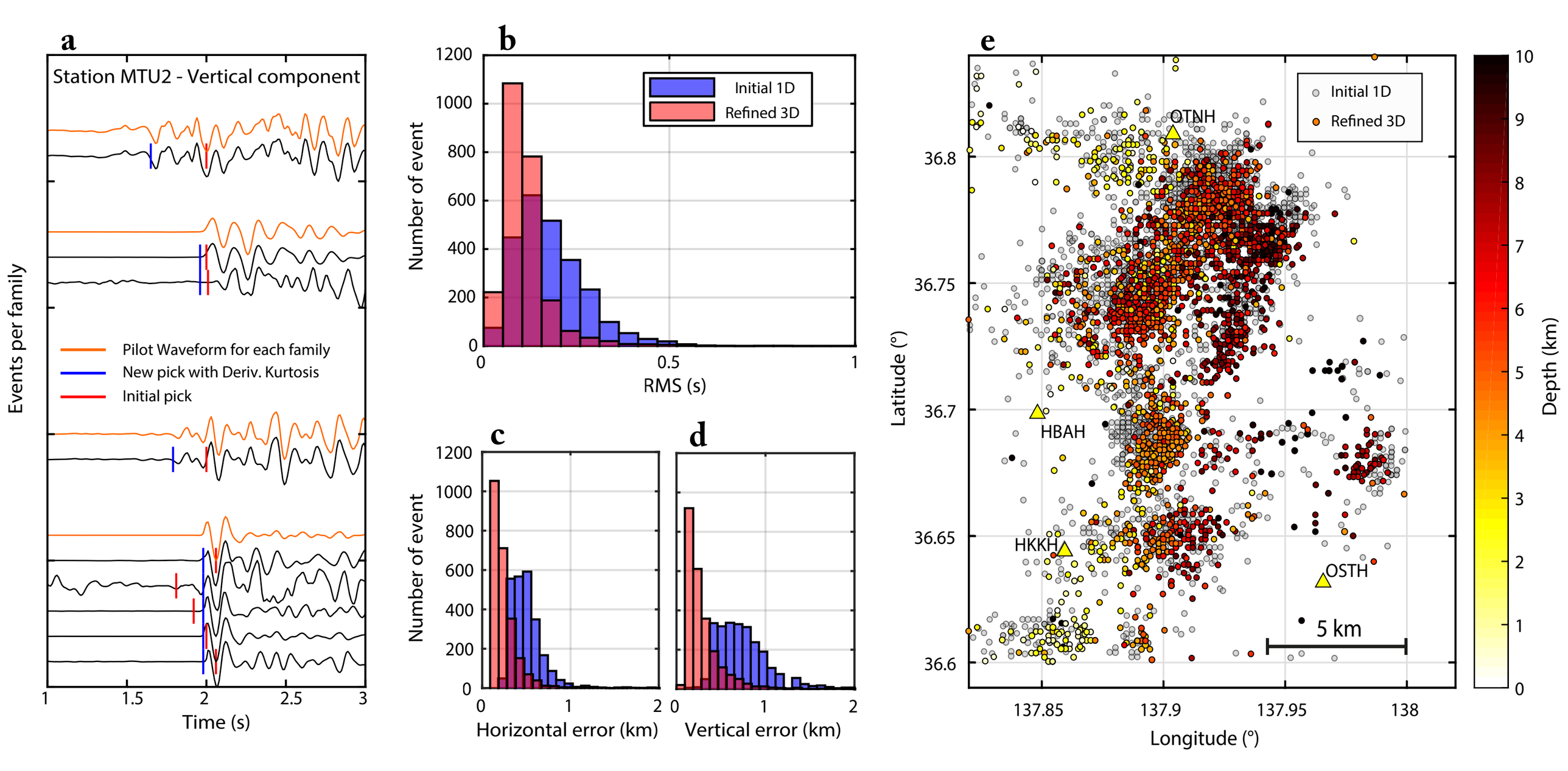
a
Station MTU2 - Vertical component
Events per family
Pilot Waveform for each family
New pick with Deriv. Kurtosis
Initial pick
1
1.5
2
2.5
3
Time (s)
b
Initial 1D
Refined 3D
Number of event
RMS (s)
c
Horizontal error (km)
d
Vertical error (km)
e
Initial 1D
Refined 3D
OTNH
HBAH
HKKH
OSTH
5 km
Latitude (°)
Longitude (°)
Depth (km)

Figure 3.

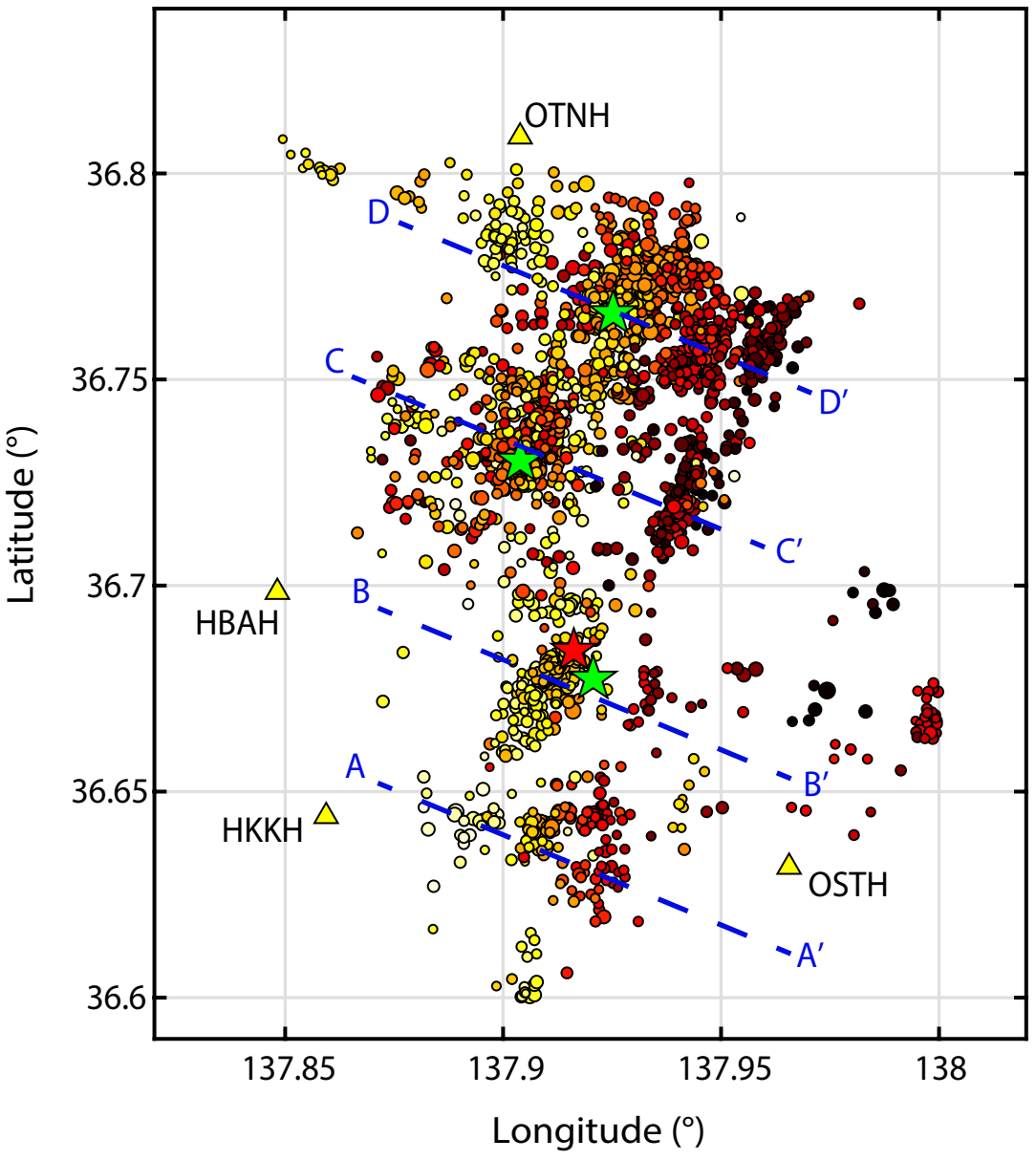
OTNH
HBAH
HKKH
OSTH
A
A′
B
B′
C
C′
D
D′
36.8
36.75
36.7
36.65
36.6
137.85
137.9
137.95
138
Latitude (°)
Longitude (°)

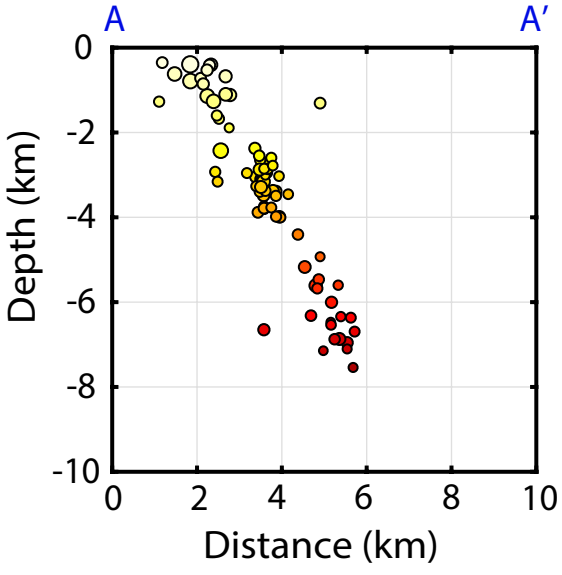
A
A′
Depth (km)
Distance (km)

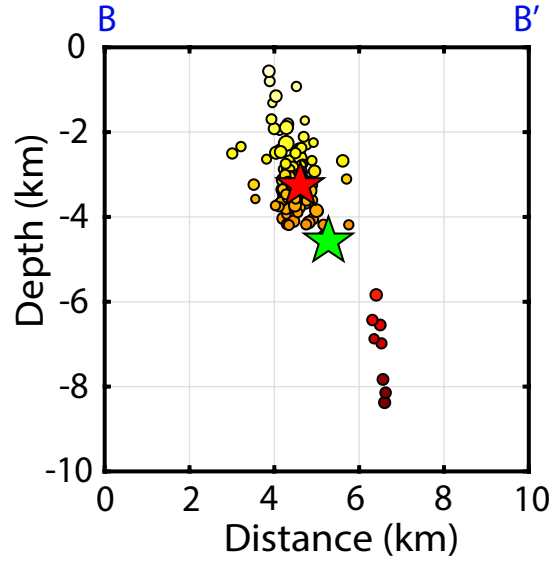
B
B′
Depth (km)
Distance (km)

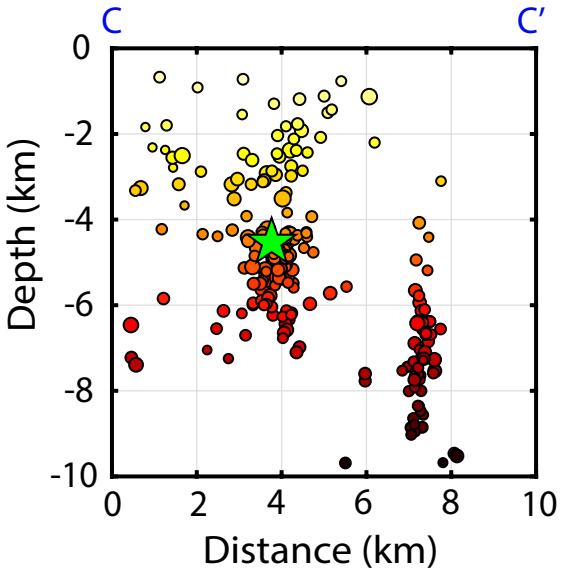
C
C′
Depth (km)
Distance (km)

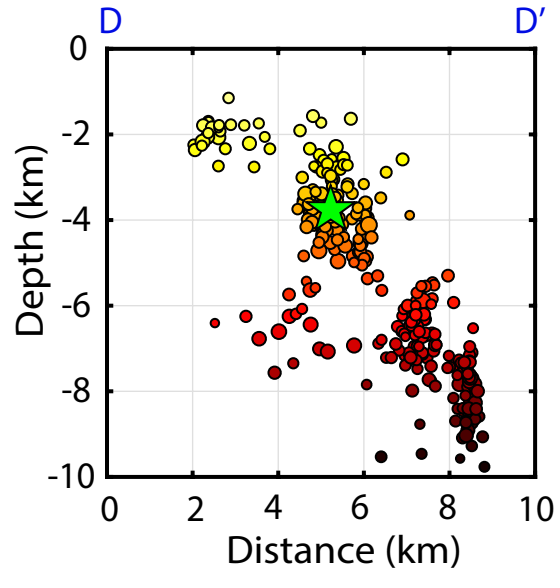
D
D′
Depth (km)
Distance (km)

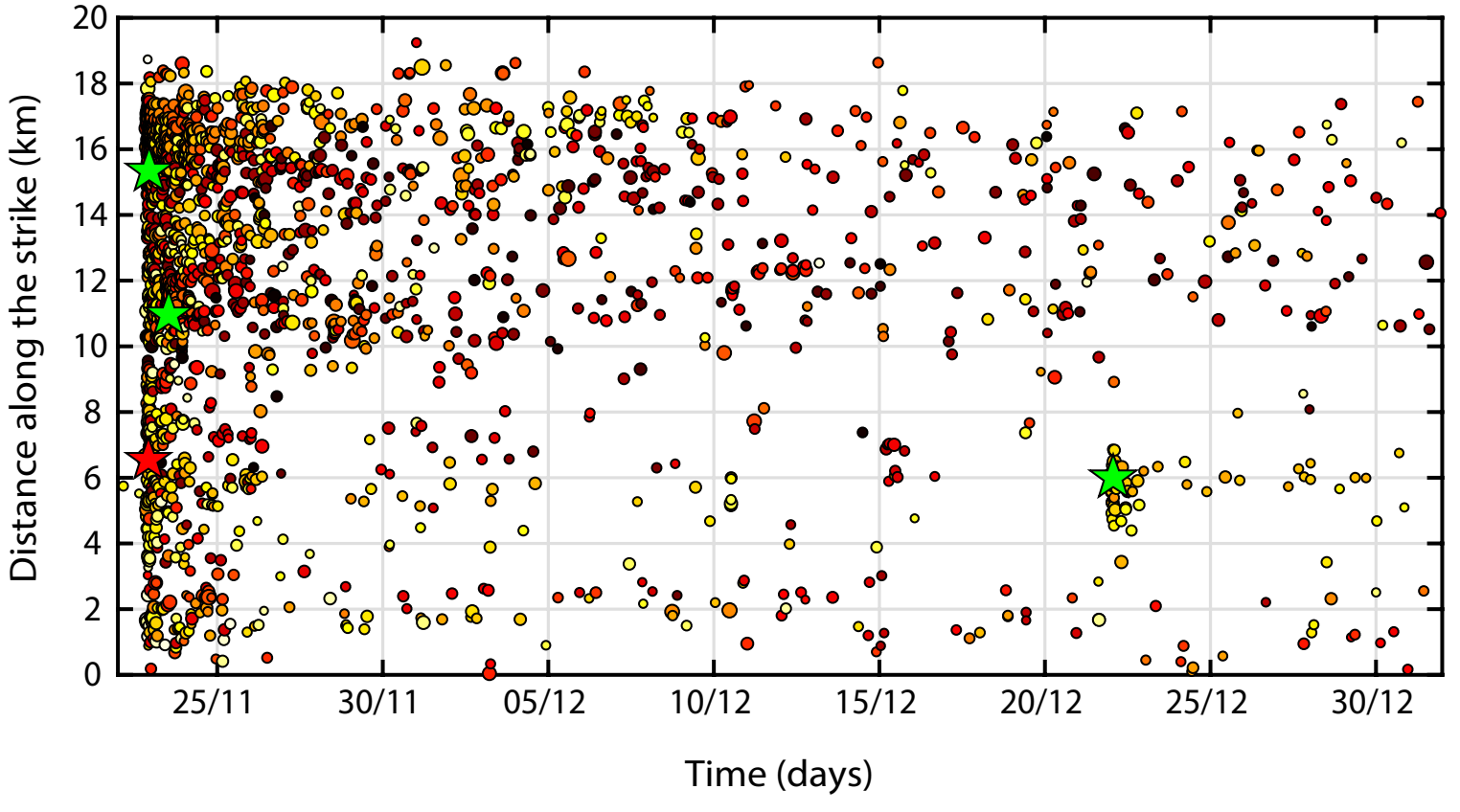
Distance along the strike (km)
25/11
30/11
05/12
10/12
15/12
20/12
25/12
30/12
Time (days)

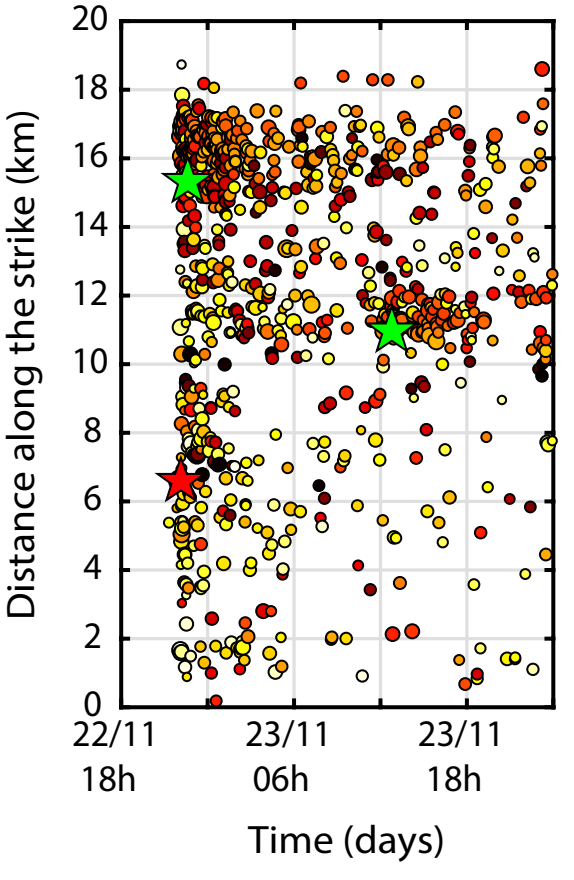
Distance along the strike (km)
22/11
18h
23/11
06h
23/11
18h
Time (days)

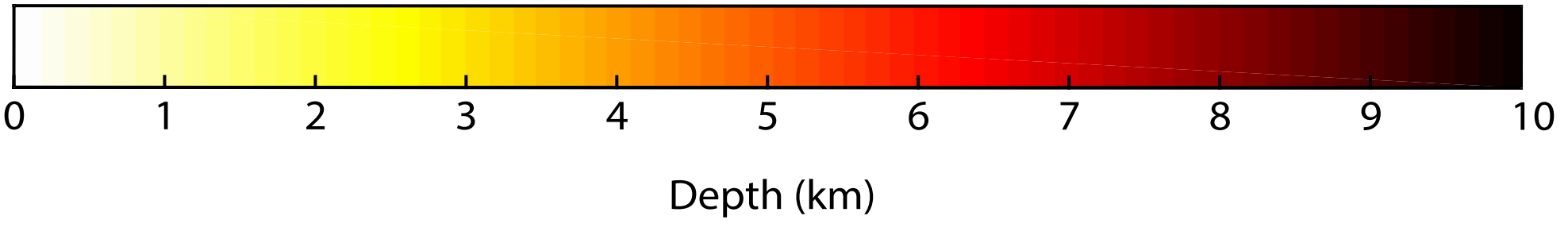
Depth (km)

Figure 4.

a
Aftershocks 1h
b
Aftershocks 3h
c
Aftershocks 12-24h
d
Aftershocks 24h - 30 Nov
e
Aftershocks 30 Nov - 31 Dec
f
OTNH
HBAH
HKKH
OSTH
A
A′
B
B′
C
C′
D
D′
Ma
5 km
Phase 1
Phase 2
Phase 3
Latitude (°)
Longitude (°)
36.8
36.75
36.7
36.65
36.6
137.85
137.9
137.95
138
0
1
2
3
4
5
6
7
8
9
10
Depth (km)

Figure 5.

Phase 1

Phase 2

Phase 2

Phase 3

Aftershocks 3h

Aftershocks 12h - 24h

Aftershocks 24h - 30 Nov

Aftershocks 30 Nov - 31 Dec

North

South

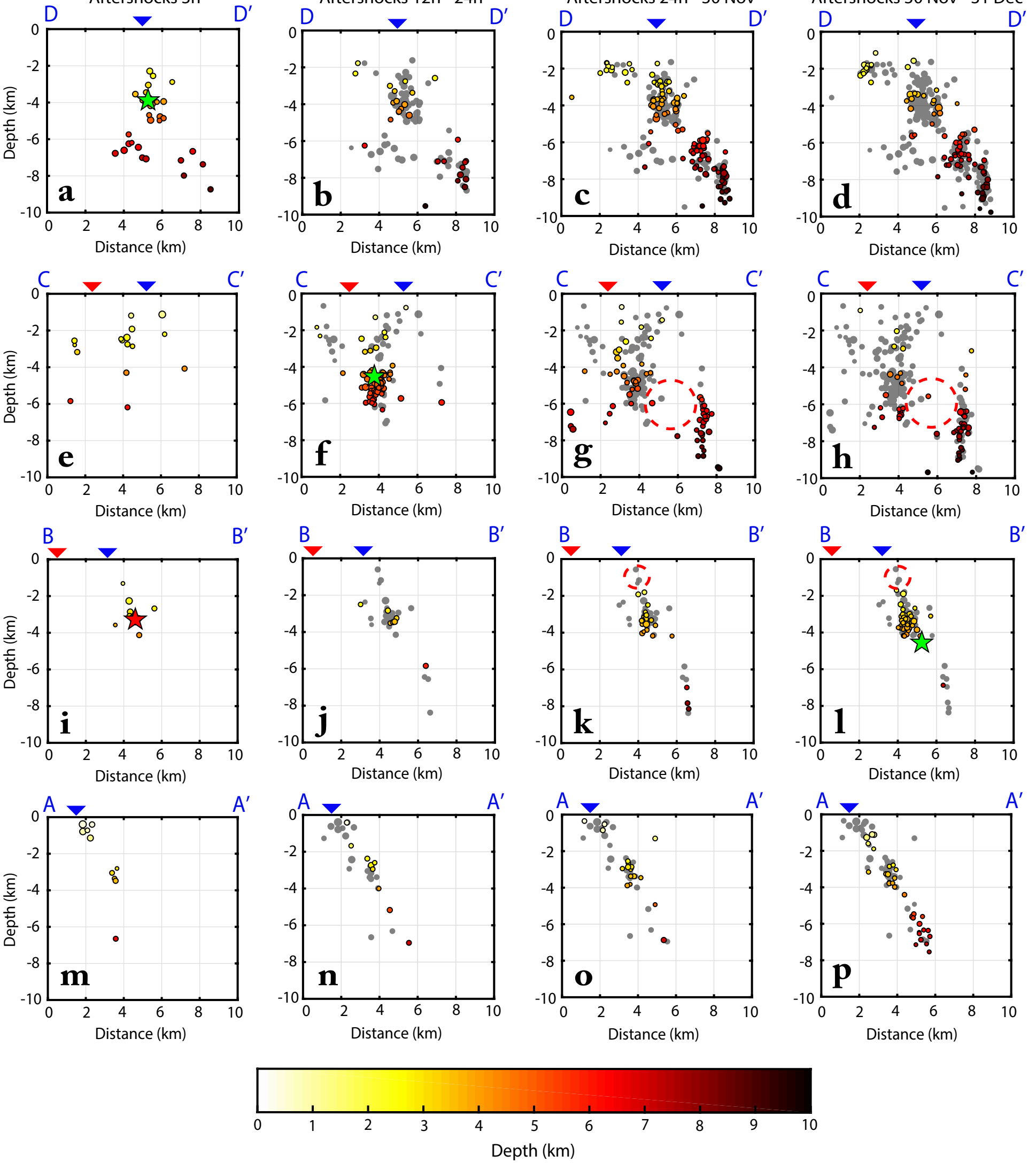

Figure 6.

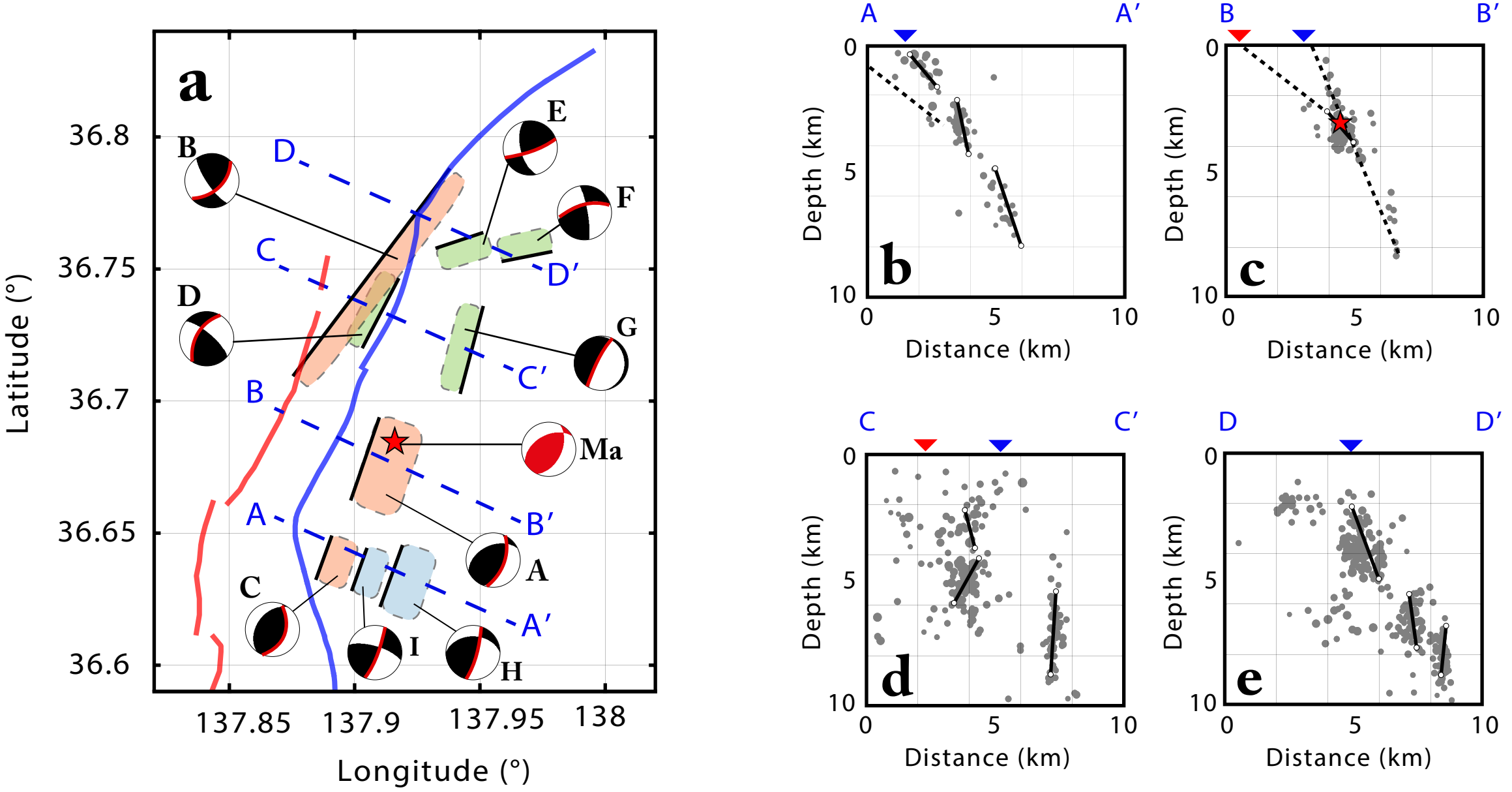
a
36.8
36.75
36.7
36.65
36.6
Latitude (°)
137.85
137.9
137.95
138
Longitude (°)
B
D
E
F
C
D′
G
C′
B
Ma
A
B′
C
A
A′
I
H
b
A
A′
Depth (km)
Distance (km)
c
B
B′
d
C
C′
e
D
D′
0
5
10

Figure 7.

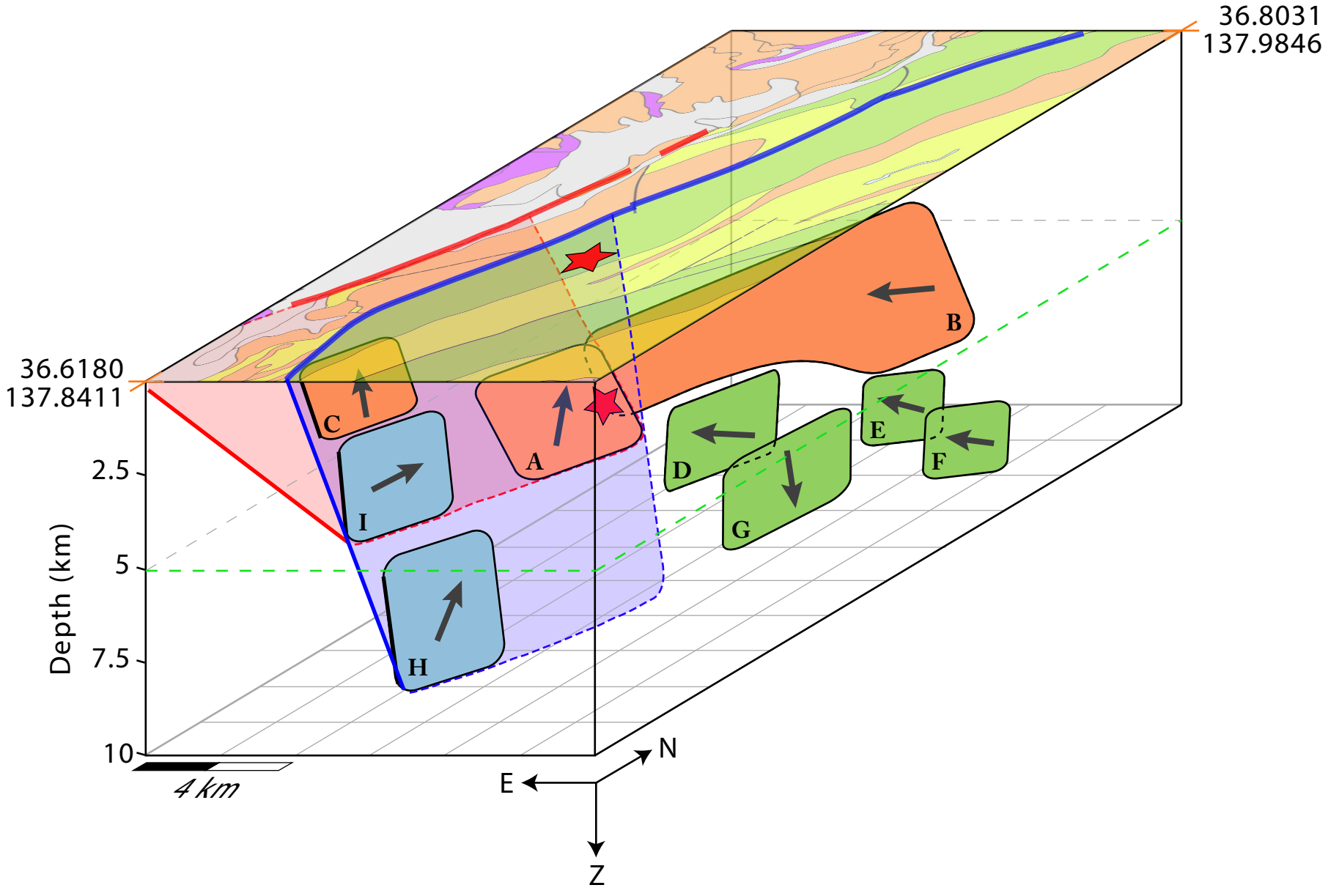
36.8031
137.9846
36.6180
137.8411
Depth (km)
2.5
5
7.5
10
4 km
A
B
C
D
E
F
G
H
I
N
E
Z

Figure 8.

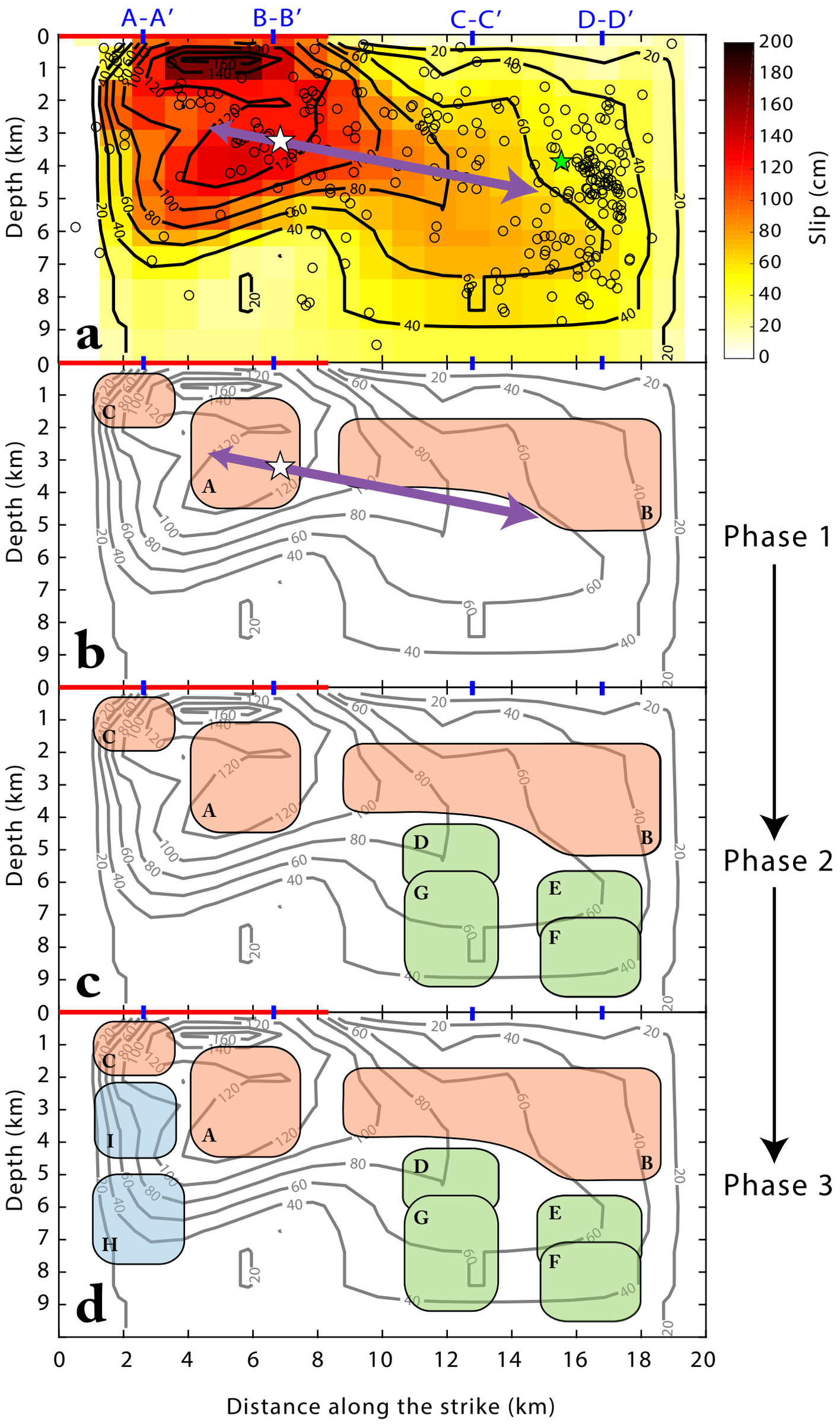
A-A′
B-B′
C-C′
D-D′
Depth (km)
Slip (cm)
200
180
160
140
120
100
80
60
40
20
0
a
b
c
d
A
B
C
D
E
F
G
H
I
Phase 1
Phase 2
Phase 3
Distance along the strike (km)
0
2
4
6
8
10
12
14
16
18
20

Phase	Time Interval	Correspondent date (UTC)
1	From MOT to 1 h after	From 14/11/22 01:08:17.56 pm to 14/11/22 02:08:17.56 pm
1	From 1 h to 3 h after MOT	From 14/11/22 02:08:17.56 pm to 14/11/22 04:08:17.56 pm
2	From 12h to 24h after MOT	From 14/11/23 01:08:17.56 am to 14/11/23 01:08:17.56 pm
2	From 24h to one week after MOT	From 14/11/23 01:08:17.56 pm to 14/11/30 11:59:59 pm
3	From one week to one month after MOT	From 14/12/01 00:00:00 am to 14/12/31 11:59:59 pm